Dissertation

MODELING AND SEMI-ACTIVE VIBRATION CONTROL OF STRUCTURES USING MAGNETORHEOLOGICAL ELASTOMERS

磁気粘弾性エラストマを用いた構造物のセミアクティブ制振とモデル化に関する研究

Kanazawa University

Graduate School of Natural Science and Technology

Division of Mechanical Science and Engineering

Student Number	**1524032017**
Name:	**Nguyen Xuan Bao**
Chief advisor:	**Prof. Toshihiko Komatsuzaki**

June, 2018

Acknowledgements

Contents

Chapter 1

Introduction

1.1 Background

Magnetorheological elastomer (MRE) is a class of smart materials that mainly generate a magnetic field dependent variable stiffness. MREs are the solid analogues [1] to MRFs composed of iron particles embedded in a low permeability carrier matrix (usually rubber). MREs are classified into isotropic and anisotropic MREs according to their curing processes. While anisotropic MREs are cured in magnetic fields, isotropic MREs are cured with1out the presence of a magnetic field. Devices that use MREs can work in multiple degrees-of-freedom (DOFs). MRE can either strain or shear through its longitudinal or lateral axis, respectively. On the other hand, devices that use MRFs only work in single DOF because an MR damper must retract and extend through its longitudinal axis. In addition, MRF devices work in post-yield areas and mainly possess tunable damping, but MRE devices also work in pre-yield areas and possess tunable stiffness. Because of variable stiffness, MRE devices can efficiently alter natural frequencies. Consequently, researchers have given interest to the application of MREs to intelligent devices in vibration control system design, such as vibration absorbers and isolators.

Vibration absorbers (VAs) have been developed to attenuate structural vibration. A traditional VA, called a passive VA, only works effectively if the frequencies of excitation are in their designed narrow band. In contrast, a VA that uses an MRE, called an adaptive-tuned vibration absorber (ATVA), is capable of adjusting the working frequency band according to the frequency of excitation in real time so that the vibrations are absorbed for a wider frequency range. For example, Komatsuzaki et al. [2] introduced an MRE of 40% iron volume content (vol%) in ATVAs in order to mitigate the vibrations of a single DOF vibration system with a frequency range of 25.8–36 Hz. In addition to the application to ATVAs, MREs are also applied to vibration isolators (VIs) used to isolate the vibration source. Similar to passive VAs, passive VIs work well in narrow designed bands. However, MRE-based VIs possess controllable stiffness whose isolation frequency can be adjusted in real time. For example, Liao et al. [3] developed an MRE-based VI where real-time semi-active vibration control techniques are applied in order to reduce vibration in the structure. The transmissibility of the payload near the resonant frequency decreased by 61.5% compared with the passive systems. The root-mean-square (RMS) values of the displacement and velocity responses also decreased significantly by 36% and 45.4%, respectively.

An MRE device is a semi-active device that requires a semi-active controller to exploit the best features of the passive and active control systems. It can be nearly as efficient as a fully active suspension system in reducing vibration without requiring the associated large power sources. It is also a safe device; even if the control fails, the device can still work as a passive suspension system. Recently, semi-active

---

control systems have emerged as smart devices and have been widely applied in vibration control (particularly vehicle suspension, earthquake protection …).

1.2 Aim and Objective of this thesis

This research aims at developing and investigating a novel MRE-based isolator. Firstly, the viscoelastic characteristics and modelling of the MRE-based isolator is conducted. Then, the new semi-active control algorithms are proposed. The seismic protection performance is evaluated numerically and experimentally by comprehensive vibration testing.

Specifically, the objectives of this research are as follows:

1) To investigate the viscoelastic characteristics of MREs in shear mode for identifying the dynamical behavior of an MRE-based isolator.

2) To propose a model which can express the viscoelastic behavior of the MRE for design vibration systems.

3) To design a new semi-active controller for an MRE-based isolator to overcome the drawbacks of traditional controllers.

4) To propose a robust adaptive controller for semi-active control of a nonlinear system with unknown dynamic parameters. The objective of the controller is to overcome the drawbacks of the conventional semi-active controller, to avoid the singularity problem, and to provide robust stability.

5) To evaluate the effectiveness of the semi-active controllers in reducing the relative displacement and absolute acceleration of the two-story shear building during seismic events in both simulation and experiment.

1.3 Contribution to Knowledge

The studies in this thesis are intended to provide a deeper insight into the characteristic of MRE-based isolator and their potential application in seismic response reduction. The new insights of this study are expected to be implemented in vibration control discipline. The novel contributions of this dissertation can be listed as follows:

1) The viscoelastic characteristics of MREs in shear mode were clarified systematically.

2) The dynamic viscoelastic model of the MRE-based isolator was presented, and a procedure to determine the six model parameters was introduced. The force-displacement relationship obtained by the numerical model is nearly consistent with the measurement results. Moreover, the proposed model predicts the dynamic viscoelastic characteristics of MRE in a wide range of frequency (3–30 Hz) and shear strain (4%–16%) with high accuracy.

3) The fuzzy semi-active vibration control with a strategy based on the Lyapunov theory was developed for minimizing the movement of the payload. The proposed strategy is fully adequate to the nonlinearity of the MRE isolator and works independently with the structure. The proposed strategy is expected to reduce the acceleration of conventional semi-active controller.

4) A robust adaptive controller is proposed for a nonlinear system with unknown dynamic parameters. The control scheme consists of three parts: a standard adaptive linearizing controller, an adaptive sliding mode controller, and a single robust controller. The proposed method guarantees zero convergence of the displacement response and provides robust stability. In addition, the singularity problem that usually appears in standard adaptive control is eliminated.

5) Simulation and experiment were performed. The results show that the isolator accompanied with a novel semi-active controller remarkably reduces the relative displacement and absolute acceleration of the two-story shear building compared to passive-off and passive-on cases during seismic events.

1.4 Thesis Organization

This thesis has been organized into seven chapters. The introduction, motivation, and innovation of this research are presented in the current chapter.

Chapter 2 presents the literature review of the whole research, the literature review relevant to each discipline area is conducted and provided in the corresponding section. The first section of this chapter provides brief fundamentals of MRE material and MRE-based isolators. Then, the previous models in earlier studies are discussed for MRE-based isolator; the advantages and drawbacks of each model are analyzed. Finally, the semi-active control algorithms are reviewed.

In Chapter 3, a novel model for capturing the dynamics behavior of MRE isolator is proposed. Firstly, the series of experiment are implemented to present the characteristic of MRE, then a model is proposed to express viscoelastic behaviors of the MRE and predict operation process of the MRE-based isolator for future design of isolator systems for various technical applications.

In Chapter 4, a semi-active fuzzy controller is designed in order to enhance the effectiveness of MRE-based isolator for 1-DOF structure. Furthermore, the semi-active fuzzy controller is conducted by using 2-storey benchmark model for evaluating the isolator performance under seismic excitation in Chapter 5.

In Chapter 6, a robust adaptive controller is proposed for a nonlinear system with unknown dynamic parameters. The new controller is expected to overcome the drawbacks of conventional robust controller.

Chapter 7 summarizes the contents of all the chapters together with concluding remarks. Some future works are also suggested in this chapter.

Chapter 2

Literature Review

2.1 Magnetorheological Elastomer and its technology

MR elastomer (MRE) was first proposed by Jolly et al. in 1996 [4]. In their research, the viscoelasticity of MRE was investigated under the presence of a magnetic field. This research presented that modulus of MRE can be changed 30%-40% by an applied magnetic field for a composite containing 30% iron particle in volume. In their study, the magneto-viscoelastic responses were presented by using a simple quasi-static dipole model. The model well fitted to the measurement over a broad range of applied magnetic field. Since then, MREs have attracted much interest not only in improving properties but also in applying the material to intelligent devices.

A basic fabrication process is described in Figure 2.1. Fabricated MRE samples consist of RTV silicon rubber, silicon oil, and iron particles with average diameter of 20μm. The materials are then placed in a mixer in order for the mixture to become homogenous. The mixture is placed in a copper mold and compressed to remove air bubbles. Finally, the mixture is cured under a magnetic field or without magnetic field at room temperature for 24 hours. While anisotropic MREs are cured in magnetic fields, isotropic MREs are cured without the presence of a magnetic field. Figure 2.2 shows the microstructure of isotropic and anisotropic MREs. The phenomenon is the consequence of magnetic force generated in magnetic particles in the curing process.

Figures 2.3 shows the microstructure of anisotropic MRE under different levels of magnetic flux density with 1600 times magnification [5]. In image (a), the iron particles are located randomly without magnetic field. From images (b)–(f), the higher value of magnetic field the thicker the chains become. It can be obvious that the thickness of particle chains depend on the intensity of magnetic field.
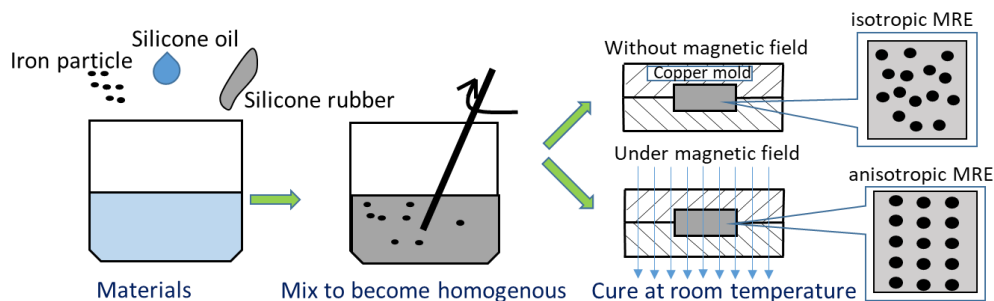
Figure 2.1: Fabrication process of MREs

(a)　　　　　　　　　　　　　　　　　(b)
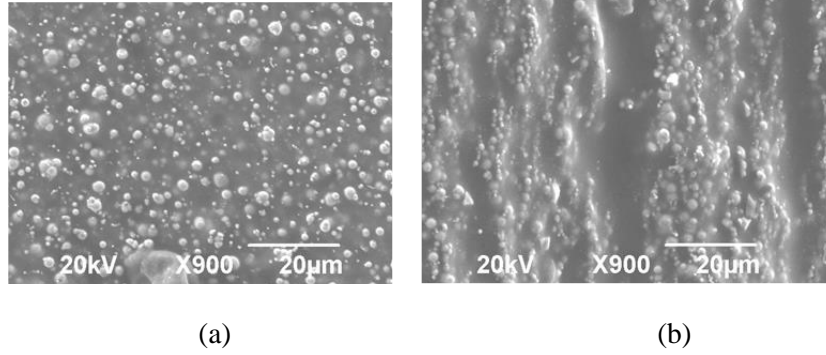
Figure 2.2: Microstructure of MRE without magnetic field: (a) isotropic, (b) anisotropic
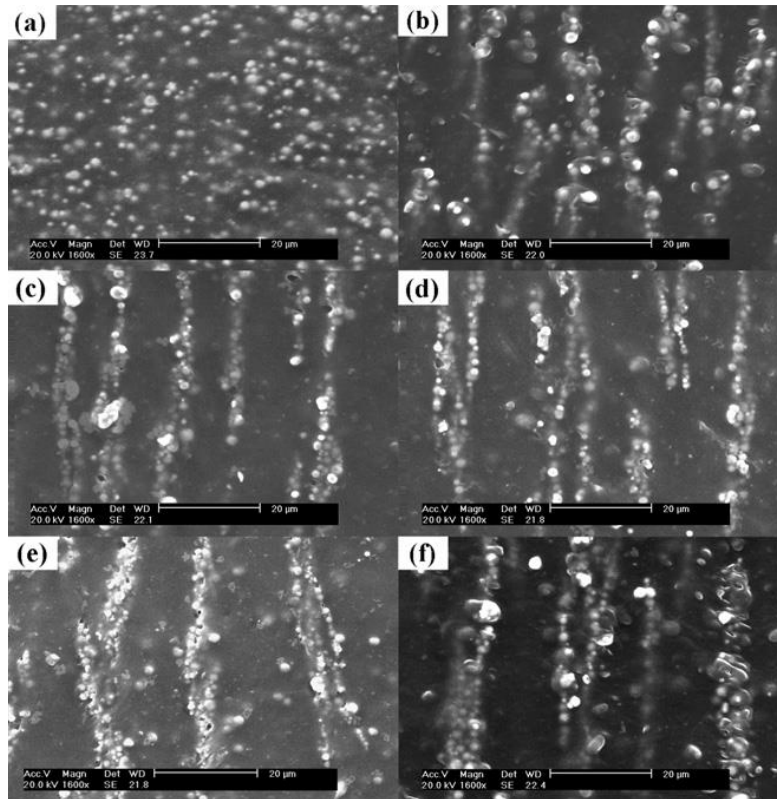
Figure 2.3. The images of MRE chains in the matrix under different levels of magnetic field: (a) to (f)correspond to from 0 to 1000 mT (with 1600 times magnification) [5].

In recent years, several researches have been reported regarding improvement and investigation of the mechanical properties of MRE [6-14]. In order to improve the properties of the MRE, many researches have focused on component materials, fabrication processes and optimal magnetic systems. For example, Gong et al. [6] investigated the effects of iron particles, additives on the MR effect, the relationship between microstructure, and mechanical properties. The silicone oil was introduced in the mixture of silicon rubber and iron particles. Therefore, the particles were easily mobilized within the elastomeric material, and their shear storage modulus was evaluated by changing their composition. Furthermore, the MRE obtains the

best properties when carbonyl iron particles, silicone rubber and silicone oil are mixed with a proportion of about 60, 20, and 20% respectively. Zang et al. [7] have proposed the fabrication process to form the patterned structure within MREs and have investigated the structural effect on their stress-strain relationship, as shown in Figure 2.4. A patterned mold, a methyl-methacrylate board with holes etched by laser was used. Firstly, the iron particles were filled into the holes of the mold. Then the thin layer polydimethylsiloxane was covered on the front surface in order to fix the position of particles. After that, they overlapped the layers to compose an MRE sample. Besides proposing the fabrication process of MRE, the electromagnetic system design so as to generate optimum magnetic field strength passing through MRE has also been emphasized. Behrooz et al. [8] proposed a variable stiffness isolator, as shown in Figure 2.11. In this isolator, the steel shim plays important roles. It helps the magnetic flux to pass through MRE layer as a channel. So, the highest magnetic field strength can be transmitted to MRE. Komatsuzaki et al. [9] developed a frequency-tunable dynamic vibration absorber, as shown in Figure 2.5. Natural frequently of the absorber can be shifted 3 times of the nominal value. A brass as an auxiliary mass with low permeability helps magnetic field becomes concentrated on the steel core and avoids leakage of magnetic field. Therefore, the system achieves the optimal magnetic field strength passing through MRE. Li et al. [10] proposed a multilayered MRE structure. The diameter of the MRE and steel sheets is 120 mm. This is a novel MRE structure that enhances significantly the mechanical properties of the MRE. The novel MRE-based isolator can significantly extend the lateral stiffness to 1630% of the base value.

The properties of MRE are clarified in [11-14, 19]. The properties are nonlinear and dependent on the frequency excitation, amplitude excitation, and magnetic field. For example, the properties of an anisotropic MRE sample ($25 \times 25 \times 10$ mm and iron content of 40 vol%) are explained in [19]. With respect to the frequency dependency, the equivalent stiffness and damping coefficient increased monotonically with the increase in frequency, as indicated in Figure 2.6. The equivalent stiffness showed an exponential increment up to the frequency of 7 Hz. Beyond 7 Hz, the equivalent stiffness increased insignificantly by increasing the excitation frequency. The damping coefficient slightly increased by the increment of frequency. The same trend was observed for different levels of magnetic field. In the amplitude dependence, the equivalent stiffness and damping coefficient are shown in Figure 2.7. The figure depicts that the equivalent stiffness decreased when the excitation amplitude increased, and the rate of this trend also increased with the increase in the current magnitude. In contrast, the change in damping coefficient was proportional to the change in excitation amplitude. The magnetic field dependence is shown in Figure 2.8. The equivalent stiffness increased sharply for the magnetic field ranging from 0 mT (0 A) to 173 mT (4 A), and the value gradually became large until it reached the saturated state when the magnetic field intensity was 365mT (6 A). The damping coefficient in Figure 8(b) showed a slight fluctuation when magnetic flux density increased, especially when the 30 Hz excitation frequency was given, but the value in overall increased gradually with

the increase in magnetic flux density until it reached saturation. The above studies concluded that MREs are the prospective materials for new engineering applications especially in the field of mechanical and structural vibration.
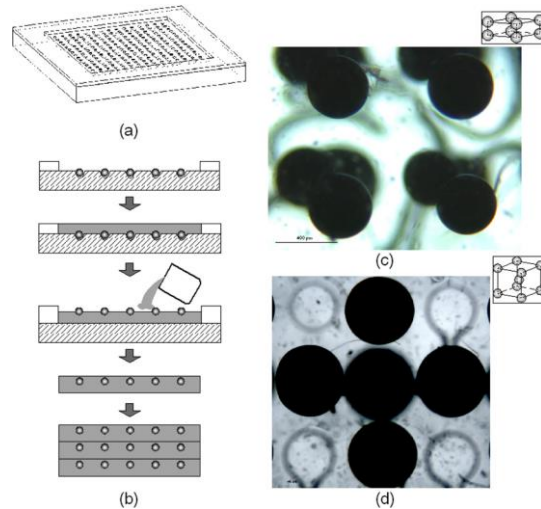
Figure 2.4: The fabrication process of MRE [7].
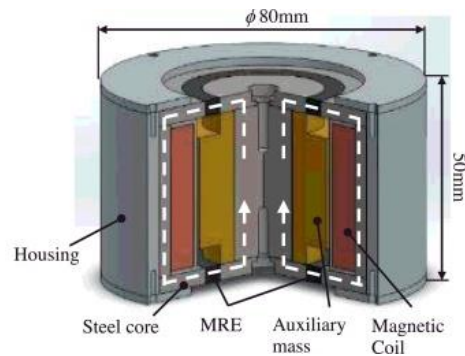
Figure 2.5 Schematic of the broadband variable stiffness DVA [9].
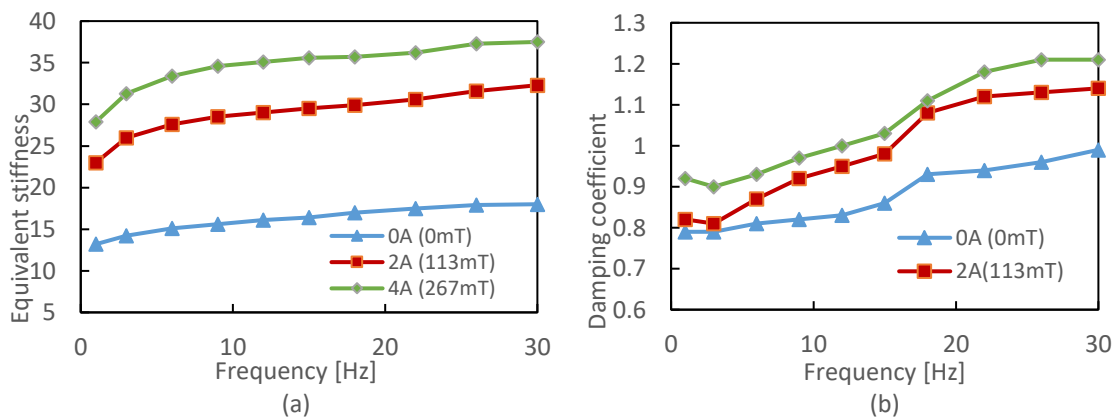
2.6 Stiffness and damping properties versus excitation frequency for different applied currents
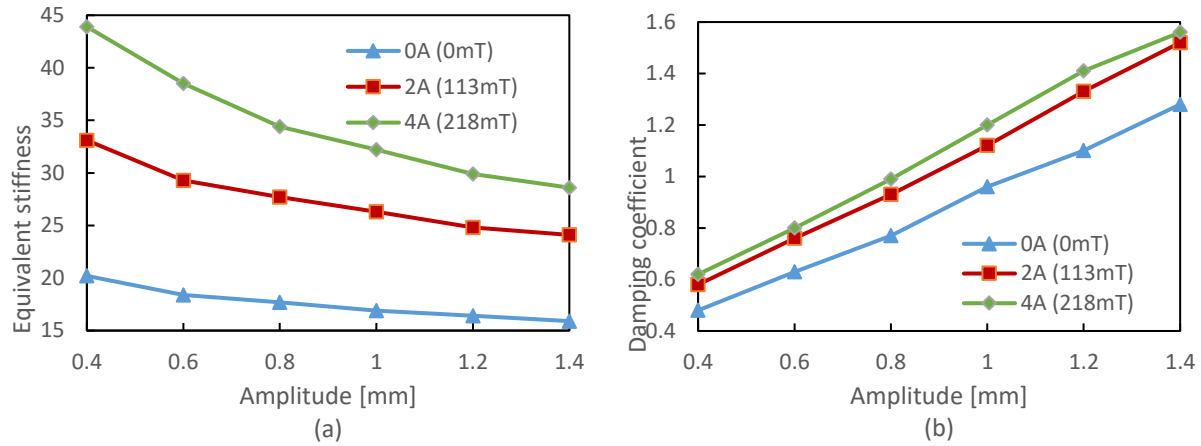
Figure 2.7 Stiffness and damping properties versus excitation amplitude for different levels of applied current.
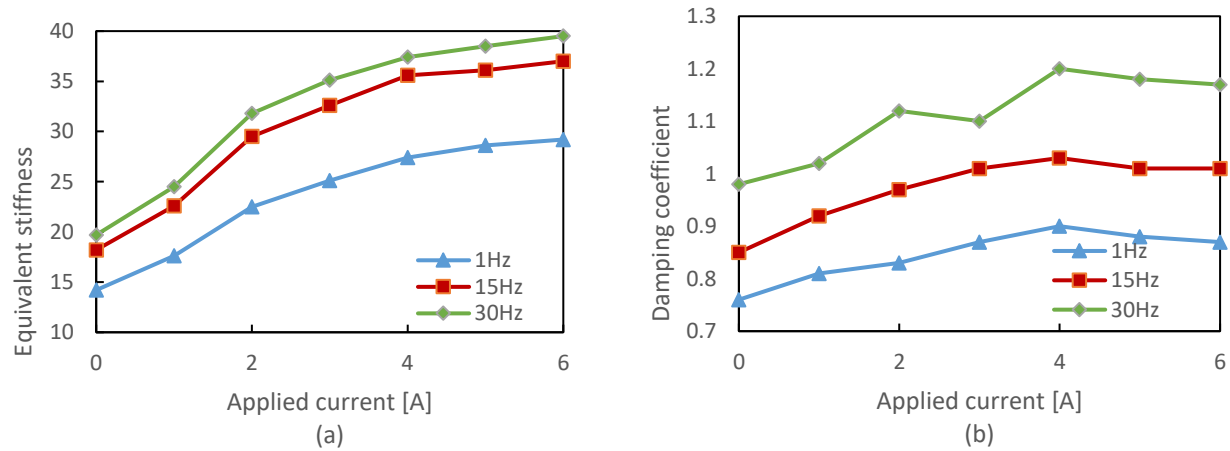
Figure 2.8 Stiffness and damping properties versus applied current (magnetic flux density) for different frequencies

2.2 MRE-based isolator

Vibration isolation is to prevent vibration energy transmission from one part to another by installing vibration isolator between them. MRE-based isolator has been intensively studied and several designs have been reported. A MRE-based isolator is a smart device that has the ability to govern the transmissibility by adjusting its properties such as stiffness and damping. This section will capture the typical MRE-based isolators for mechanical engineering application.

Liao et al. [15] developed a tunable stiffness and damping vibration isolator based on MRE. The stiffness can be adjusted by varying the applied magnetic field, as shown in Figure 2.9. By using this isolator, the vibration of the payload with the controller was significantly suppressed in whole frequency range dealt

in experiment. The relative displacement was decreased by 61.5 % at the resonant frequency. The displacement transmissibility decreased from 2.6 to about 1. Obviously, the vibration isolation system performed efficiently.

Jung et al. [16] developed the smart base-isolator using MRE, as shown in Figure 2.10. A single-story structure was used to investigate numerically as well as experimentally the effectiveness of the isolator under earthquake loading. Their research has shown that the MRE based-isolator combined with the fuzzy controller reduced significantly the relative responses of structure.
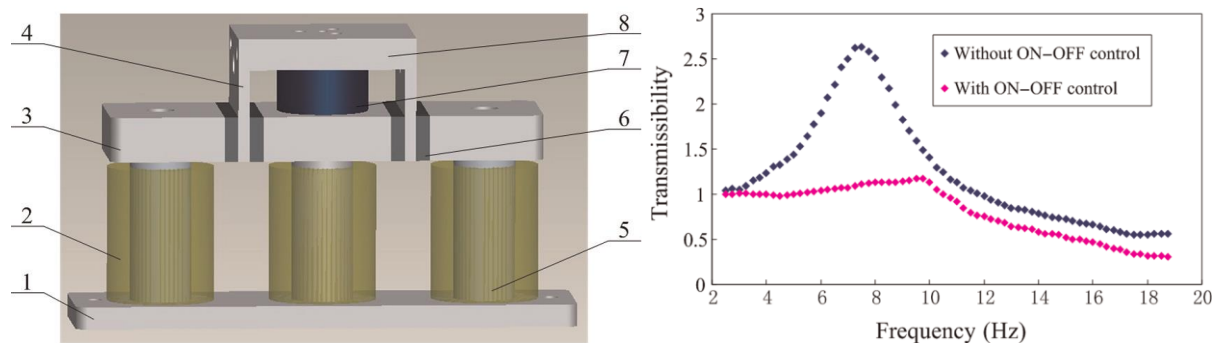
Figure 9. The MRE-based vibration isolator [15] : (a) Sketch of the isolator, (b) Frequency response to base excitations.
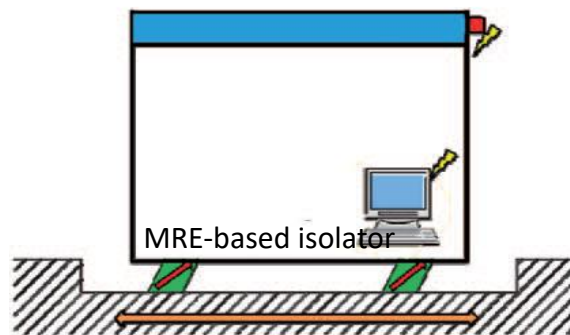
Figure 2.10. A building with MRE-based isolator [16].

Behrooz et al. [17] proposed an isolator as shown in Figure 2.11. The two caps were placed at top and bottom of the MRE material. The power cord realizes positive and negative currents in order to magnetic field is closed-loop. By this way, the optimal magnetic field was generated, resulting in large stiffness variation range. The VSDI equipped with a Lyapunov-based controller worked well for the scaled building in seismic response reduction.

Li et al. [10] proposed a highly adjustable MRE-based isolator, as shown in Figure 2.12. The isolator used a soft MRE that traditional laminated rubber bearing and sheet steel were incorporated. The new MRE

based isolator possesses significant adaptability, such that the restitution force increases up to 1470% and stiffness to 1630% when the applied current is increased from 0A to 3A. The isolator is suitable to cope with earthquake excitations with reliability and efficiency.
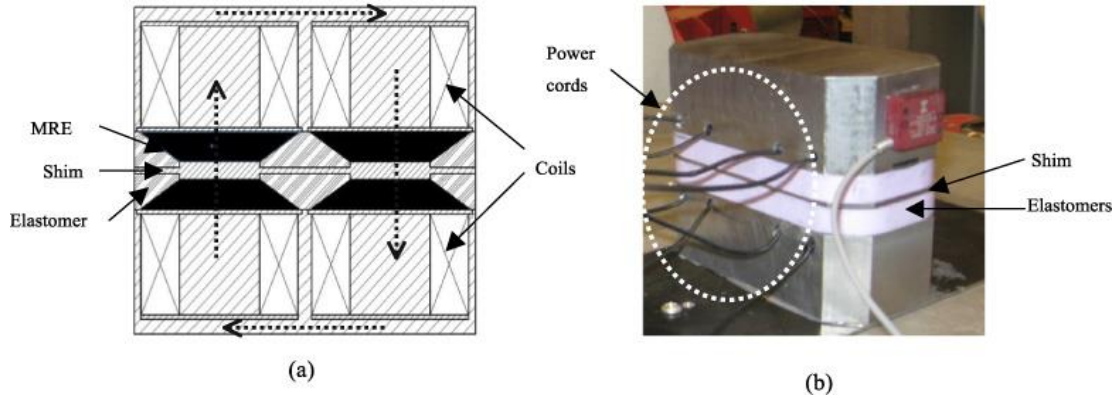
Figure 2.11. (a) Schematic of the isolator, and (b) photo of the isolator [8, 17].
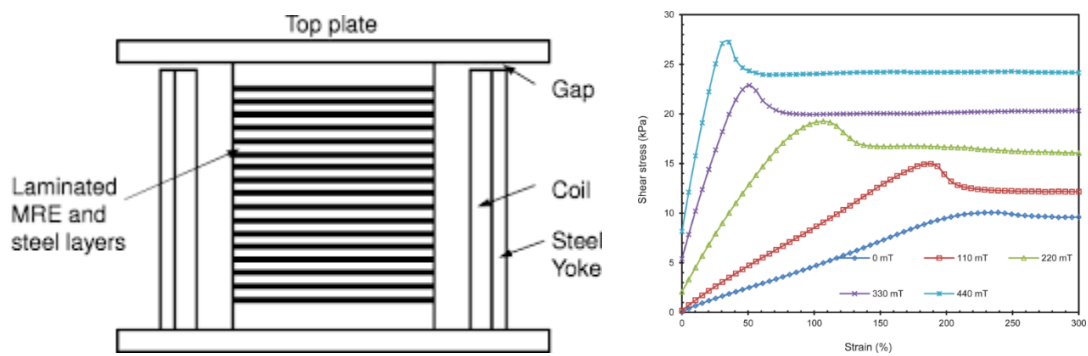
Figure 2.12 The highly adjustable MRE-based isolator [10].
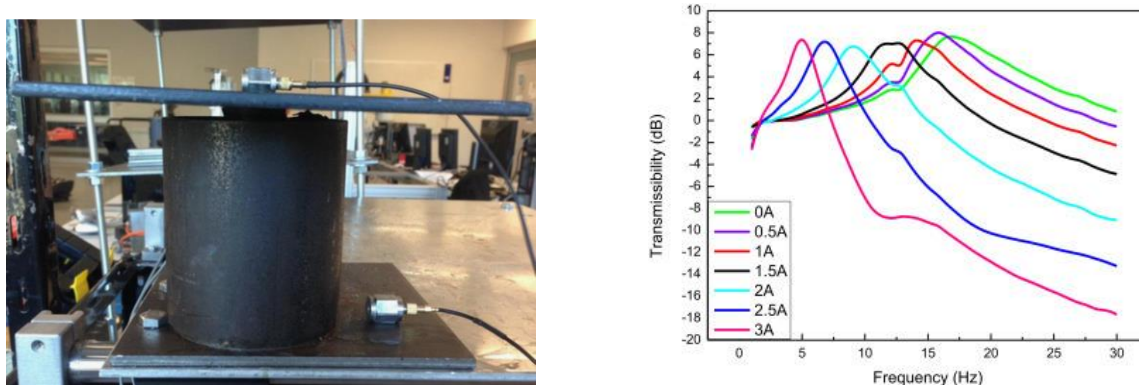
Figure 2.13 The MRE-based isolator [18]: (a) the photograph, (b) the natural frequency was shifted from 5Hz to 20 Hz.

Yang et al. [18] developed a novel multi-layer MRE isolator for suppression of building vibrations. In their research, the laminated structure consisted of 10 layers of soft MRE alternating with 11 layers of steel sheets, as shown in Figure 2.13. The novelty of the isolator is using a permanent magnet at the top and bottom of this laminated structure. The research proved that the novel isolator accompanied with fuzzy controller was effective for semi-active control.

2.3 Modelling of MRE-based isolator

In order to design MRE-based isolator systems for various technical applications, a numerical model is necessary to represent dynamic behaviors of MRE. Unfortunately, these behaviors are strongly nonlinear functions of magnetic flux density and displacement amplitude, and they are also affected by changes in frequencies to some extent [19]. Therefore, modeling of the MRE properties is a substantial challenge, particularly in vibration control technology. Recently, MRE modeling has been considered in two aproaches: micro model and macro model.

In the microscopic modeling, the change of chains of iron particles under the change of magnetic field strength were considered [20, 21]. Chen et al. [20] proposed a finite-chains model to capture the relationship between the microstructures and the viscoelastic properties. The sketch of the model is shown in Figure 2.14. In this model, the particles structure is changed under different level of magnetic fields. The shear stress is calculated based on the continuum mechanics. The computational result agrees well with the experiments. Li et al. [21] proposed a micromechanics-based viscoelastic model with chain structure that predicted magnetic-field-dependent dynamic shear stiffness and damping of MRE. In their research, the iron particles were assumed to form spherical blocks with appropriate ratios. These blocks interact with the free matrix elastomer, as schematically shown in Figure 2.15.

The macroscopic modeling is based on stress–strain (or force–displacement) relationship of MREs in different levels of amplitudes, frequencies, and magnetic fields. Li et al. [22] developed a four-parameter viscoelastic model for MRE, as shown in Figure 2.16. In this model, a spring element is in parallel with the standard Kelvin-Voigt model that represents the viscoelastic properties of MRE under harmonic loadings. However, the strain amplitude is limited below 10% and frequency is less than 10 Hz. The four parameters are determined based on the least squares method to minimize the error between the measurement and simulation results.
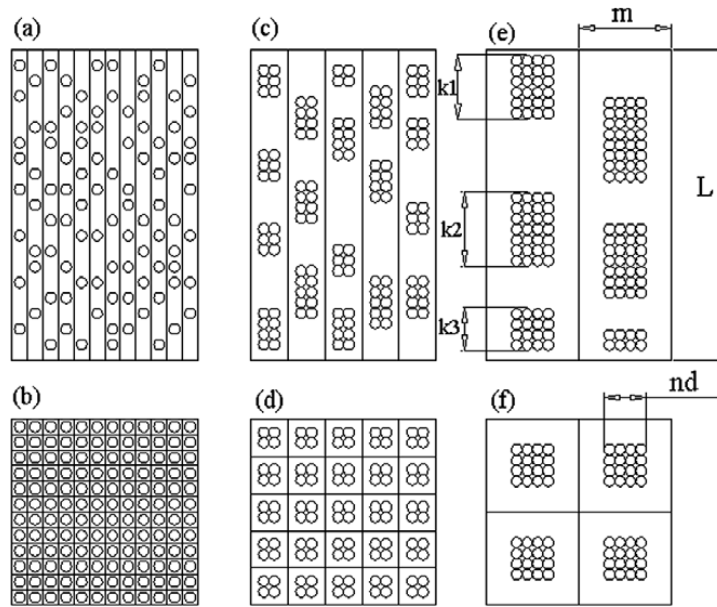
Figure 2.14. MREs' finite-chains model [20]. The iron particles (white circles) was shaped under difference levels of magnetic field strength: (a, c, e) correspond to zero magnetic, low value of magnetic and strong value of magnetic respectively. (b), (d), and (f) are cross sections.
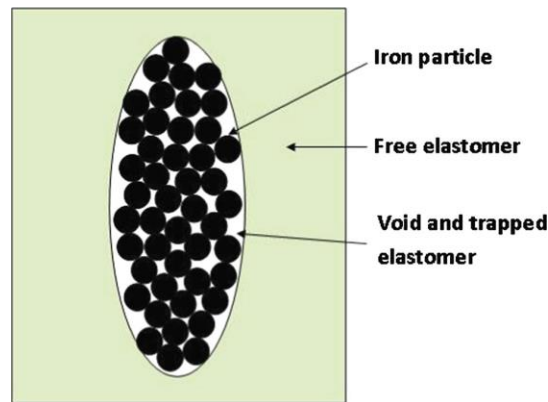
Figure 2.15 The microstructures model of MREs [21].
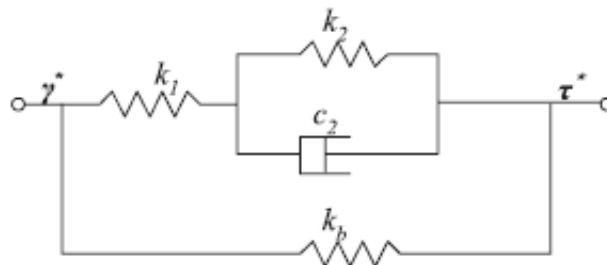
Figure 2.16 Four-parameter viscoelastic model for MR elastomers [22].

Eem et al. [23] developed a nonlinear dynamic model that combined the Ramber-Osgood model and the Maxwell model, as shown in Figure 2.17. Simple algebraic equations were used to represent hysteretic nonlinearity. The parameters of the shear deformation of the MRE were determined by using a Nerder-Mead optimization algorithm.
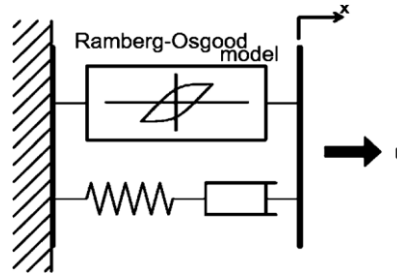
Figure 2.17. The MRE-based isolator model with Ramberg-Osgood model [23].
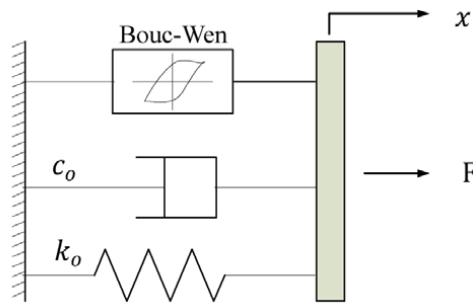
Figure 2.18. Schematic diagram of the MRE-based isolator model [24].

The Bouc-Wen model is well acceptable in MRE modeling in recent years [24]. The Bouc-Wen component is placed in parallel with a Voigt element, as shown Figure 2.18. The Bouc-Wen part represents the hysteresis loops, while the Voigt part represents the solid-material behaviors. In parameter identification, six parameters were determined by a least-square method in combination with the Trust-region-reflective algorithm. The algorithm minimized the vector of the value of the root mean square error.

A non-linear model that the modulus and damping are the nonlinear functions of frequency, amplitude and value of magnetic field was developed for MRE [25], Figure 2.19.
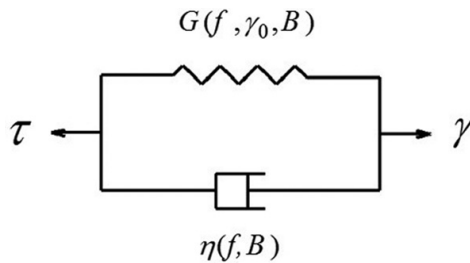
Figure 2.19. The nonlinear model for MREs [25].

2.4 Semi-active control

The MRE-based isolator is one of the semi-active devices that require an efficient controller. Because of nonlinearity in the model, not many control algorithms exist that could effectively operate MRE devices. The following semi-active control algorithms are usually used in recent years.

Consider a 1-DOF vibration system with an MRE as a tunable stiffness element. The motion equation is described as,

$$m\ddot{x} + c\dot{x} + k_{MRE}x = c\dot{u} + ku \tag{2.1}$$

In Eq. (2.1), x represents the displacement of mass m, u is the displacement of the ground base, c is the MRE damping coefficient, $k_{MRE} = k_{min} + \Delta k$ is the tunable MRE stiffness, k_{min} is the minimum stiffness which is obtained without applied current, and Δk is the increment stiffness when the current is applied.

The open-loop algorithm is the simplest and cheapest way to perform a control. The control algorithm is set in advance and the feedback of the state variables is not necessary. The controller performs as a passive controllers with different value of stiffness. The stiffness can be switched from a net value to another one. However, the frequency of the system must be known in advance. This controller can be used widely for vibration isolator of rotating machineries, such as washing machines, tool machines, and suspension vehicle. For example, for washing machines, the high stiffness value is set when the drum operates at low speed, while the low stiffness value is set for high speed. The switching rule for stiffness can be defined as follows,

$$k_{MRE} = \begin{cases} k_{min} & f < f_{min} \\ k_{\max} & f \geq f_{max} \end{cases}, \tag{2.2}$$

where k_{min} and k_{max} is the minimum and maximum stiffness values of an MRE, f_{min} and f_{max} are the minimum natural frequency and maximum natural frequency, respective.

The on-off skyhook algorithm [26, 27] has been extensively used in MRE devices. In these cases, the stiffness is adjusted to either a high or a low value according to the measured relative displacements. The algorithm is summarized as,

$$k_{MRE} = \begin{cases} k_{min} & x\dot{x} \geq 0 \\ k_{max} & x\dot{x} < 0 \end{cases}, \tag{2.3}$$

where x and $\dot{x}$ are the relative displacement and relative velocity, respectively.

The logic of the on-off skyhook control mechanism is explained as follows: when the system tends to leave the equilibrium position ($x\dot{x} < 0$), isolators produce maximum force ($F = \Delta k_{max}x$) to absorb

vibration as much as possible; in contrast, if the system tends to return to the equilibrium position ($x\dot{x} \geq 0$), the isolator with on-off semi-active controller does not produce external force ($F = 0, k = k_{min}$); then the system returns to equilibrium position freely.

In the on-off skyhook algorithm, the high and low stiffness are defined as a constant stiffness values. The algorithm can be replaced by the continuous skyhook algorithm. The low stiffness remains defined by a constant stiffness value, while high stiffness value is set equal to a continuous gain value,

$$k_{MRE} = \begin{cases} k_{min} & x\dot{x} \geq 0 \\ \alpha & x\dot{x} < 0 \end{cases}, \tag{2.4}$$

where α is the continuous function that depend on the relative responses and the value is not exceeding the corresponding high and low stiffness limits, $k_{min} \leq \alpha \leq k_{max}$.

Regarding the other semi-active algorithms, consider a seismically excited multi-degree-of-freedom structure to be controlled, for which the equation of motion can be written as follows,

$$M\ddot{x} + C\dot{x} + Kx = \Lambda f - M\Gamma\ddot{x}_g \tag{2.5}$$

Defining the state vectors as $z = [u \quad \dot{u}]^T$. The equation can be written in state-space form as

$$\dot{z} = Az + Bf_{MRE} + E\ddot{x}_g, \tag{2.6}$$

where *M, C*, and *K* represent $(n \times n)$ mass, damping, and stiffness matrices, respectively; x is the vector of the displacements of the masses relative to the ground; f is the measured force generated by semi-active device; $\ddot{x}_g$ is ground acceleration; Λ is the matrix determined by the placement of control devices; Γ is the column vector of ones.

The clipping control algorithm for the system represented by Eq. (2.5) is used in [28]. The controller is divided into two stages: an ideal active controller and a passive controller in which the control variable is switched by a "clipped on-off" algorithm. In the ideal active control laws, the control algorithms, such as PID control, LQG control, optimal control, H_2 or H_∞ control, can be used. To clip the active controller the following clipped on-off algorithm is usually used,

$$v = V_{max}H[(f_c - f)f] \tag{2.7}$$

where v is the command voltage, $H(.)$ is the Heaviside step function, V_{max} is the maximum voltage applicable to the isolator to achieve the maximum stiffness value, f_c and f are the desired force and measured force, respectively.

The Lyapunov control algorithm [17] determines the control voltage to minimize the derivative of the Lyapunov function. For the system represented by Eq. (2.5), the Lyapunov function can be chosen that is a positive definite function of the states as following,

$$V(x) = \frac{1}{2} z^T P z \tag{2.8}$$

where P is a symmetric, real positive definite matrix defined by

$$AP + A^T P = -Q \tag{2.9}$$

The Lyapunov function is derivative as,

$$\dot{V}(x) = -\frac{1}{2} z^T Q z + z^T P B f \tag{2.10}$$

The voltage command based on the force measurement, can be determined to minimize the $\dot{V}(x)$

$$v = V_{max} H(-z^T R B f) \tag{2.11}$$

where H is the Heaviside step function.

The Bang–Bang controller [29] is introduced to dissipate energy in the structure. The Lyapunov function is chosen as energy of vibration

$$V = \frac{1}{2} x^T K x + \frac{1}{2} (\dot{x} + \Gamma \dot{x}_g)^T M (\dot{x} + \Gamma \dot{x}_g) \tag{2.12}$$

The derivative of the function is,

$$\dot{V} = \frac{1}{2} x^T K \dot{x} + \frac{1}{2} (\dot{x} + \Gamma \dot{x}_g)^T M (-C\dot{x} + Kx + \Lambda f) \tag{2.13}$$

The Bang-Bang control algorithm is developed to minimum $\dot{V}$ (maximizing energy dissipation). The following control algorithm is chosen

$$v_i = V_{max} H(-(\dot{x} + \Gamma \dot{x}_g)^T \Lambda_i f_i) \tag{2.14}$$

where Λ_i is the ith of the Λ matrix.

In these algorithms, the applied command current/voltage is set at either the minimum or the maximum value states. Consequently, chattering will be caused that could inversely affect the system's quality. However, the current/voltage associated with a suitable command may lie between the maximum and minimum values. The semi-active fuzzy control algorithm [19, 30, 31] can generate a continuous control output. The controller overcomes the chattering and effectively reduces the structural response of the buildings. The input variables are the relative displacement (x) and the velocity $(\dot{x})$ of the first floor. The

input are divided into two intervals of linguistic variables: negative (Neg) and positive (Pos). As the control output, tunable stiffness (k^*) is divided into high stiffness (High) and low stiffness (Low). The membership functions are depicted in Figure 2.20. Fuzzy rules play an important role in a fuzzy control system and are listed in Table 1.1.
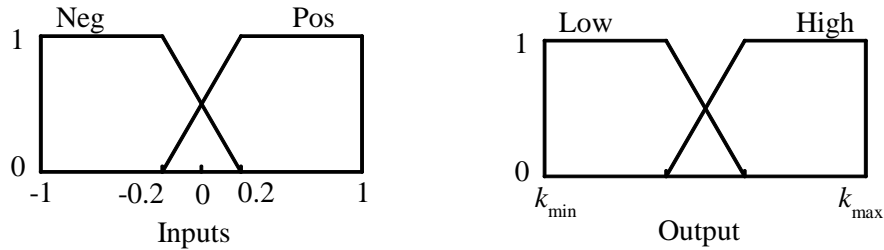
Figure 2.20 Fuzzy logic membership functions

Table 1.1 Fuzzy logic rules.

Relative displacement/ Velocity	Neg	Pos
Neg	High	Low
Pos	Low	High
Fuzzy inference	Mamdani type	
De-fuzzification	Center of gravity	

In the algorithms mentioned above, the command current/voltage is determined based only on the measured relative displacement and velocity responses without considering the dynamical behavior of the system. Moreover, uncertainties may exist in the structural parameters, such as the material inhomogeneity, nonlinearity components, changing load environment, and disturbances. Consequently, these controllers may exhibit unsatisfactory isolation performance, and even cause instability. To overcome these drawbacks, the design of a robust controller for the nonlinear dynamic system is necessary.

Chapter 3

Properties and Modelling of MRE-based isolator

In order to design MRE-based isolator systems for various technical applications, a numerical model is necessary to represent dynamic behaviors of MRE. Unfortunately, these behaviors are strongly nonlinear functions of magnetic flux density and displacement amplitude, and they are also affected by changes in frequencies to some extent. Recently, different viewpoints of MRE modeling were considered [6-10]. However, these models only worked effectively in the low-frequency range and narrow range of excitation amplitude. Besides that, determining the parameters of the model was complex.

In this chapter, the viscoelastic characteristics of MREs in shear mode are first clarified systematically in order to achieve a mathematical basis for the model development. Then, a numerical model that expresses viscoelastic behaviors of the MRE and predicts operation process of the MRE-based isolator for a future design of isolator systems for various technical applications is proposed. Despite the simplicity in parameter definition in comparison to the conventional models, the proposed model works efficiently in a wide range of frequencies and amplitudes. The model consists of the following components: viscoelasticity of host MRE , magnetic field-induced property, nominal viscosity in conjunction with high stiffness property in low excitation frequency that are modeled in analogy with a standard linear solid model (Zener model), a stiffness variable spring, and a smooth Coulomb friction, respectively.

3.1 Experimental setup

The experiment is setup to clarify the viscoelastic characteristics of MREs in shear mode and identify the proposed model parameters. Fabricated MRE samples consist of Room Temperature Vulcanization (RTV) silicone rubber (high-trength condensation-cure type, Shin-etsu KE1416), silicone oil, and iron particles (BASF SG-BH) with an average diameter of 20 μm. The materials were placed in a mixer for the mixture to become homogenous. The mixture was then placed in a copper mold and compressed to remove air bubbles. Finally, the mixture was cured under a magnetic field of 0.5 T for 24 hours. An anisotropic elastomer sample was formed in square cuboids of sides 25 mm, thickness 10 mm, and iron content of 40 vol%.

The measurement setup is shown in Figure 3.1. An electromagnet consists of iron cores and a magnetic coil. A wire of diameter 1 mm is used to wind the coil in 800 turns. Two MREs are placed in the gaps between upper and lower cores of the electromagnet. In these gaps, a magnetic flux density was varied from 0 mT to 326 mT in response to a current change from 0 A to 6 A, respectively. While the lower core is installed on a base exposed to excitation, the upper core is fixed along a load sensor. The base is excited by a shaker with excitation signal supplied by a signal generator and a power amplifier. The displacement of

the base and upper core's force are measured using a laser displacement sensor and a load sensor, respectively. The force-displacement response is processed by a Fast Fourier Transform (FFT) spectrum analyzer. A direct current (DC) power supply provides adjustable direct current to a magnetic coil. In dynamic tests, numerous experiments were conducted for various harmonic inputs. The excitation frequency was adjusted from 1 Hz to 30 Hz, excitation amplitude was changed from 0.4 mm to 1.4 mm, and applied current was driven from 0 A to 6 A (magnetic flux density was adjusted from 0 mT to 326 mT).

(a)

(b)
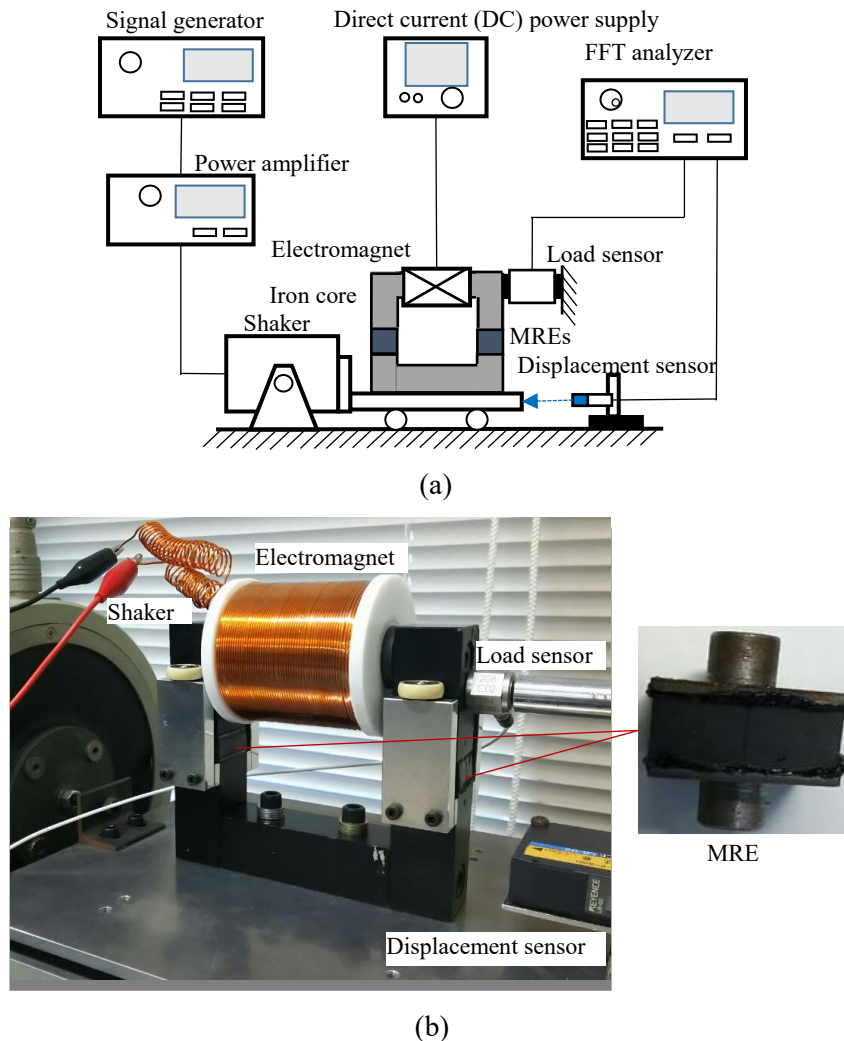
Figure 3.1 MRE viscoelastic property measurement system: (a) schematic, and (b) photograph.

3.2 Properties of MRE

The properties of MRE are depicted by force-displacement loops as shown in Figure 3.2. Three displacement amplitudes are considered: small amplitude, 0.4 mm; medium amplitude, 1.0 mm; and large amplitude, 1.4 mm. Measurements are performed for two levels of frequency: low frequency, 1 Hz; and medium frequency, 15 Hz. As can be seen in Figure 3.2(a), there is an existence of the hysteresis loop at

low frequency. The loops maintain their shape if the excitation frequency is relatively low, and therefore present a nominal viscous behavior in MRE. The slope of the hysteresis loops increases as the excitation amplitude decreases, thus the equivalent stiffness increases in small amplitude. The nominal viscosity as well as the increasing stiffness in small amplitude are similar to frictional behaviors. It is shown in Figure 3.2(a) that the tangent of the loop for $x \gg -x_0$ or $x \ll x_0$ (segment d), where x_0 denotes the displacement amplitude, approaches a constant value especially in large excitation amplitude. Thus, the nominal stiffness is linear. Figure 3.2(b) shows that the hysteresis loops become more elliptical with increasing frequency. The increasing stiffness as well as the hysteresis being more elliptical with the increasing frequency are due to the frequency-dependent viscous effect. Therefore, the viscous property of MRE consists of the nominal viscosity and the viscosity affected by frequency. Consequently, the MRE generates a nonlinear viscous behavior besides the linear stiffness. The similar trends are also observed for all values of applied currents. The MRE properties, which depend on excitation frequency, excitation amplitude, and magnetic flux density, are clarified in [19].
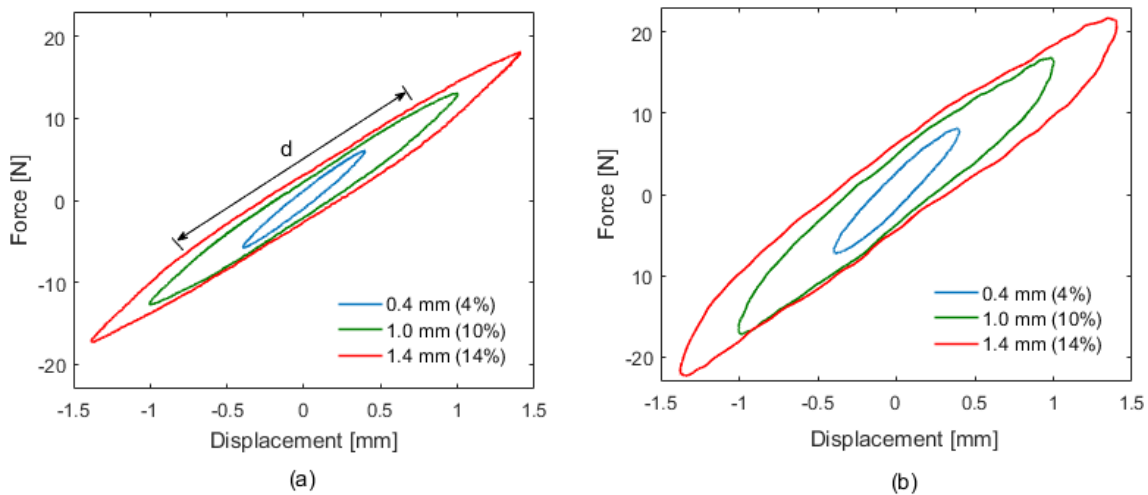
Figure 3.2 Force-displacement response for MRE to harmonic excitations: (a) low frequency (1Hz), (b) medium frequency (15Hz).

3.3 Proposed model of MRE-based isolator

In order to represent the dynamic properties of the MRE deforming in shear direction, a dynamic system was modeled, as shown in Figure 3.3. The model consists of a standard linear solid model, a stiffness variable spring, and a smooth Coulomb friction. A standard linear solid model consists of the Maxwell model in parallel with a linear spring, so that the frequency-dependent viscosity and the linear stiffness property of the host MRE can be represented. The relationship between force and displacement can be described as follows:

$$F_1 = K_1 x, \tag{3.1}$$

$$F_2 = C\dot{x}_1, \tag{3.2}$$

$$F_2 = K_2(x - x_1), \tag{3.3}$$

$$F_v = F_1 + F_2, \tag{3.4}$$

$$\Delta E_v = \frac{\pi \omega C}{1 + (\omega / \omega_v)^2} x_0^2, \tag{3.5}$$

where K_1 is the linear spring component of the material, K_2 is the spring constant of stiffness component in Maxwell model, C and x_1 are the coefficient and displacement of the viscous component, respectively. F_1 and F_2 are the elastic force and the viscous force, F_v and x correspond to the viscoelastic force and displacement of the component, ΔE_v is the loss energy per cycle caused by the viscoelastic force , $\omega_v = K_2/C$ is the characteristic frequency, and ω is the harmonic excitation frequency.

Eq. (3.5) is rewritten as follows.

$$\Delta E_v = \frac{\pi C}{1/\omega + \omega/\omega_v^2} x_0^2, \tag{3.6}$$

According to Cauchy's inequality, the denominator part of Eq. (3.6) represents the minimum value $2/\omega_v$ at the characteristic frequency $\omega = \omega_v = K_2/C$. Consequently, the loss energy, ΔE_v, reaches the maximum value of $0.5\pi K_2 x_0^2$.

When MRE is exposed to a magnetic field, the embedded ferromagnetic particles are magnetized. The force of variable stiffness generated by the MRE-based isolator with magnetic flux density, F_m, is expressed as,

$$F_m = K_m x, \tag{3.7}$$

$$\Delta E_m = 0, \tag{3.8}$$

where K_m is the variable stiffness, ΔE_m is the loss energy per cycle caused by the force.

The nominal viscosity as well as the increasing stiffness at small amplitude can be expressed by using a friction force. Note, however, that the Coulomb friction function needs to be smoothed to be able to run the simulations. Therefore, the smooth Coulomb friction model [38] is considered as,

$$F_f = F_{fs} + \frac{x - x_s}{x_2(1 - \text{sgn}(\dot{x})\alpha) + \text{sgn}(\dot{x})(x - x_s)} \left(F_{f\ max} - \text{sgn}(\dot{x})F_{fs}\right). \tag{3.9}$$

$$\Delta E_f = 2F_{f\ max} \left(2x_0 - x_2(1+\alpha)^2 \ln \frac{x_2(1+\alpha) + 2x_0}{x_2(1+\alpha)}\right), \tag{3.10}$$

where $F_{f\,max}$ is the maximum friction force, x_2 is the displacement needed for the friction force to reach $F_f = F_{f\,max}/2$, ΔE_f is the loss energy per cycle caused by the friction, F_{fs} and x_s are the friction force and the displacement at static equilibrium, respectively; $\alpha = F_{fs}/F_{fmax}$ is an auxiliary quantity ranging from -1 to 1, and $sgn(\dot{x})$ denotes the signum function of the displacement rate.

Since three forces are generated in the standard linear solid model, in the stiffness variable spring, and in smooth Coulomb friction element, connected in parallel, the total force F, the energy E, and the loss of energy ΔE per cycle, can be expressed as follows,

$$F = F_v + F_m + F_f, \tag{3.11}$$

$$\Delta E = \Delta E_v + \Delta E_f, \tag{3.12}$$

$$E = \int_0^{x_0} F dt. \tag{3.13}$$

The equivalent stiffness K, and the loss factor L, are defined by the following equations,

$$K = \frac{F_0}{x_0}, \tag{3.14}$$

$$L = \frac{\Delta E}{E}, \tag{3.15}$$

where F_0 is the force amplitude and x_0 is the displacement amplitude.
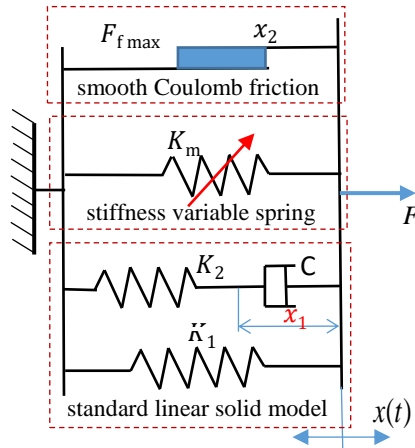
Figure 3.3 MRE component model: a standard linear solid model, a stiffness variable spring, and a smooth Coulomb friction connected in parallel.
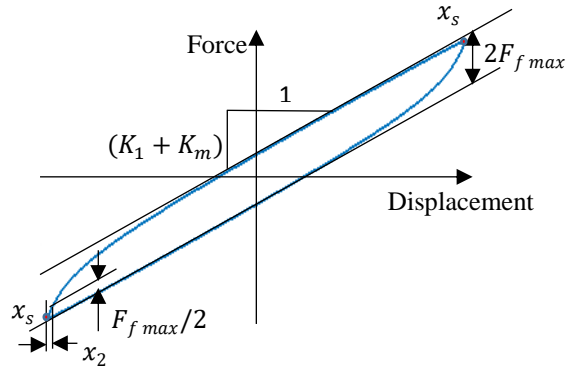
Figure 3.4 Definitions of the model parameters: K_1, K_m, $F_{f\,max}$, and x_2.
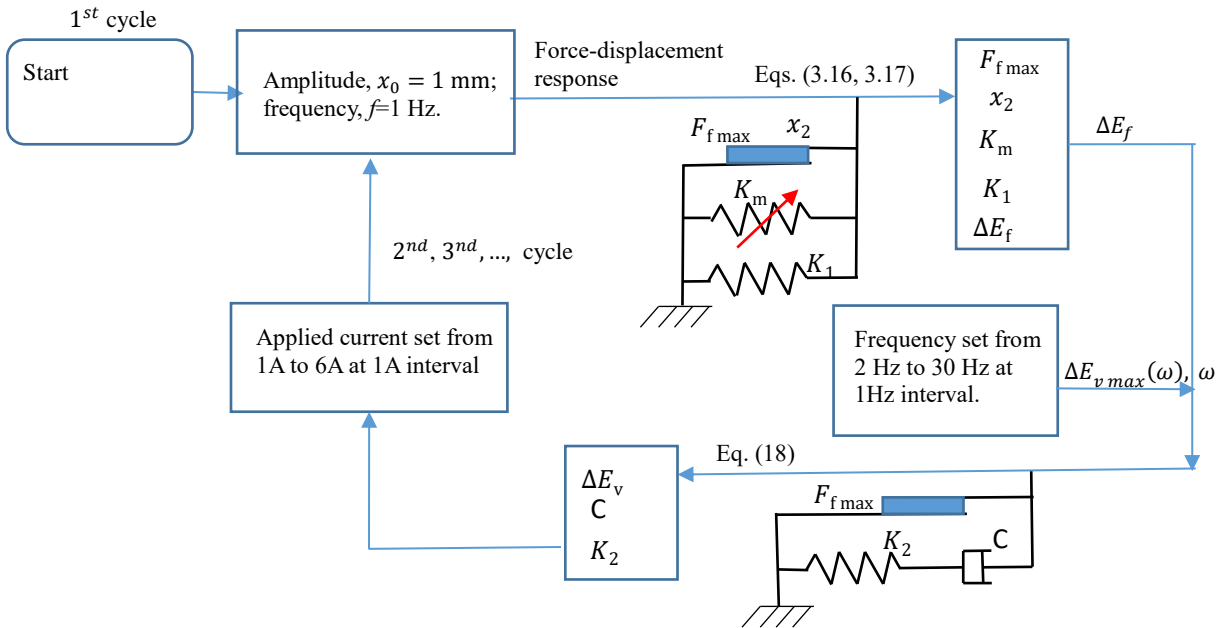
Figure 3.5 Proposed identification steps of the model parameters in MRE modeling

Table 3.1 Parameters defined for different applied current values

	0 A	2 A	4 A	6 A
K_1 [N/mm]	13	13	13	13
K_2 [N/mm]	9	9	9	9
C [N.s/mm]	0.035	0.035	0.035	0.035
K_m [N/mm]	0	6.5	11	11.5
F_{fmax} [N]	2.4	6.5	9.5	10
x_2 [mm]	0.09	0.09	0.09	0.09

3.4 Determination of model parameters

The parameters are determined according to the following procedure, from step 1 to step 3.

Step 1: Determination of the model parameters, $K_1, K_m, F_{f\ max}$, and x_2.

The displacement amplitude, $x_0 = 1$ mm and excitation frequency, $f=1$ Hz, were selected for experiment. The force-displacement curve is shown in Figure 3.4. In the case of low excitation frequency, the viscous effects modeled by Eqs. (3.2) and (3.5) become extremely small and can be neglected ($F_2 \approx 0, E_v \approx 0$). When displacement is $x \gg x_s$ or $x \ll x_s$ (x_s is the static equilibrium), the friction force, represented by Eq. (3.9), becomes maximum ($F_f = F_{fmax}$). The total force and loss energy per cycle in Eqs. (3.11) and (3.12) are rewritten as,

$$F = (K_1 + K_m)x + F_{f\ max}, \tag{3.16}$$

$$\Delta E = \Delta E_f, \tag{3.17}$$

where $F(x)$ is the force determined by measured force-displacement loop, and ΔE is the loss energy per cycle determined by the area enclosed by the loop, K_1 is the nominal stiffness of MRE without magnetic field, and K_m is the increment stiffness when the electric current is applied. Consequently, K_1, K_m, F_{fmax}, and ΔE_f are calculated, where x_2 is used to determine the rate of friction force development relative to the displacement. The parameters are illustrated in Figure 3.4.

Step 2: Determination of the viscosity parameters, K_2 and C.

Under the constant displacement amplitude $x_0 = 1$ mm, frequency was varied from 2 Hz to 30 Hz at 1 Hz interval. From the experiments, the maximum loss energy $\Delta E_{max}(\omega)$ is used for determining model parameters. From Eq. (3.10), the friction loss energy (ΔE_f) is found to be independent of excitation frequency. The viscous loss energy, modeled by Eq. (3.6), is dependent on frequency and reaches maximum at characteristic frequency $\omega = K_2/C$,

$$\Delta E_{v\ max}(\omega) = 0.5\ \pi\omega K_2 x_0^2 = \Delta E_{max}(\omega) - \Delta E_f, \tag{3.18}$$

where $\Delta E_{max}(\omega)$ and $\omega = K_2/C$ are the maximum loss energy and the characteristic frequency determined by experimental results. ΔE_f is determined by Eq. (3.17) in step 1. The model viscosity parameters, K_2 and C are then identified.

Step 3: Redo step 1 and step 2 for different applied currents.

The proposed procedures are schematically displayed in Figure 3.5. The identified parameters are shown in Table 3.1. From the table, the model parameters such as K_1, K_2, C, and x_2 are found to change insignificantly by the applied currents. On the other hand, the parameters K_m and $F_{f\ max}$ increase

significantly on increasing current. From the values in Table 3.1, K_m and $F_{f\ max}$ are approximated by the following continuous function.

$$K_m = -0.38I^2 + 4.25I, \ F_{f\ max} = -0.24I^2 + 2.75I + 2.4 \ \ I \in [0,6] \tag{3.19}$$

Consequently, the model parameter values and the approximation formulae were identified as listed in Table 3.2.

Table 3.2 Parameter for the proposed MRE model

Stiffness (K_1)	13 Nmm^{-1}
Stiffness (K_2)	10 Nmm^{-1}
Viscous damping (C)	0.035 Nsm^{-1}
Friction displacement (x_2)	0.09 mm
Maximum friction force ($F_{f\ max}$)	$F_{f\ max} = -0.24I^2 + 2.75I + 2.4$
Variable stiffness (K_m)	$K_m = -0.38I^2 + 4.25I$
Applied current (I)	$I \in [0,6]$ Ampere
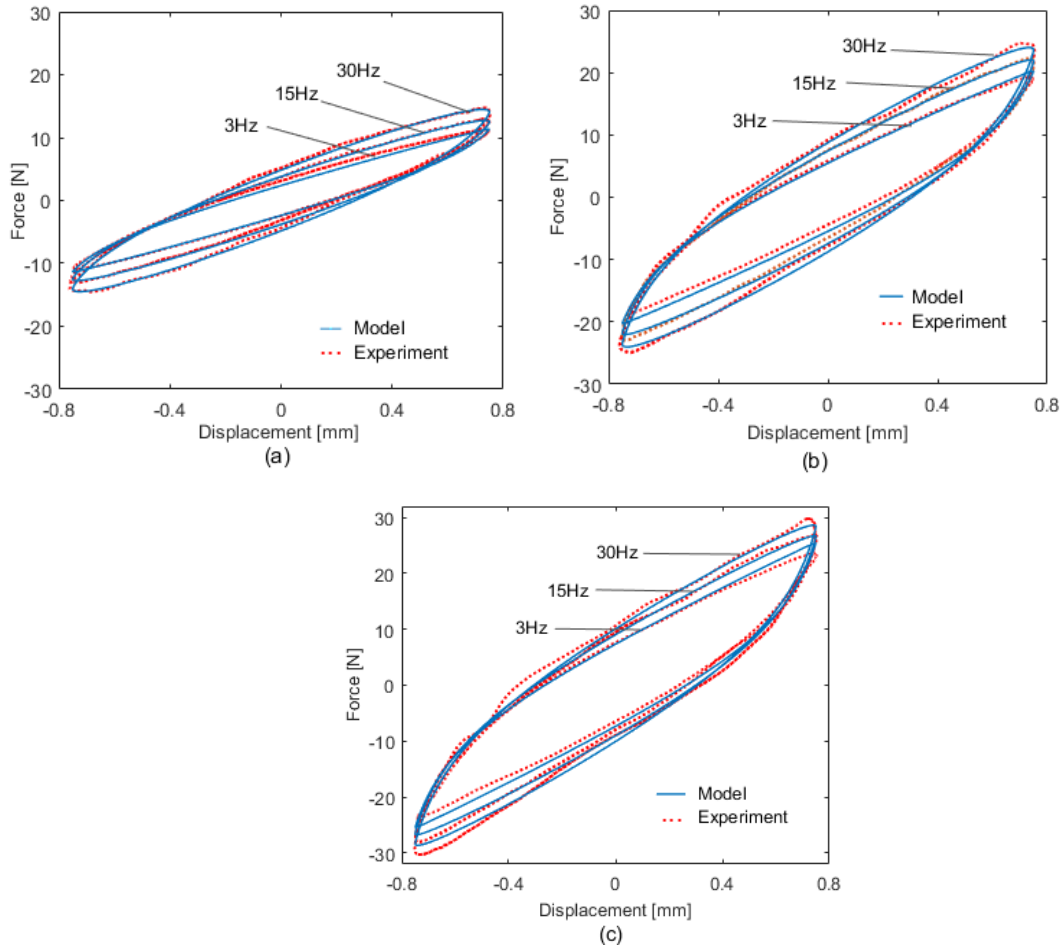
Figure 3.6 Force-displacement response under different frequencies with excitation amplitude $x_0 = 0.75mm$: (a) $I = 0$ A (0 mT), (b) $I = 2$ A (218 mT), and (c) $I = 4$ A (267 mT).
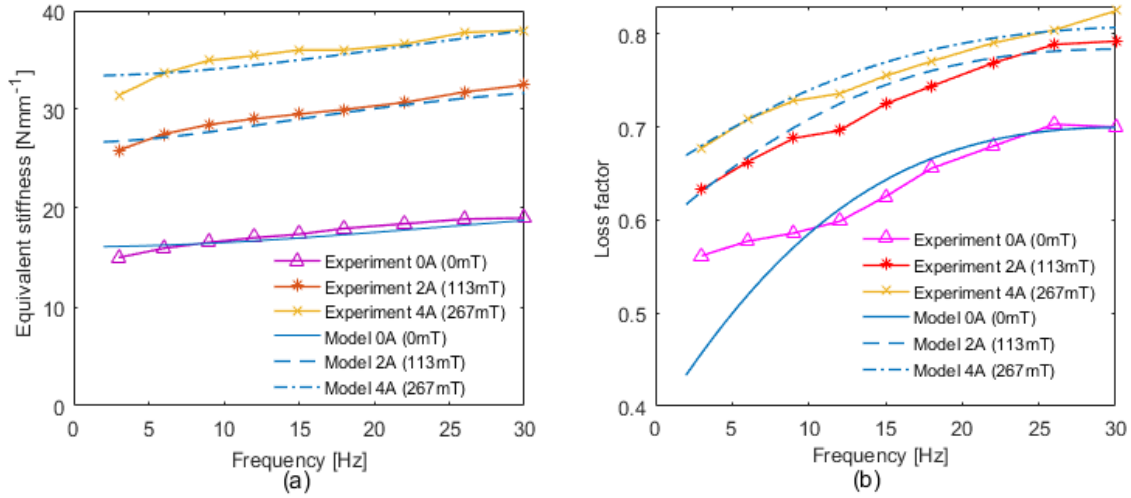
Figure 3.7 Stiffness and loss factor versus excitation frequency for different applied currents with excitation amplititude $x_0 = 0.75$ mm: (a) the equivalent stiffness and (b) the loss factor.
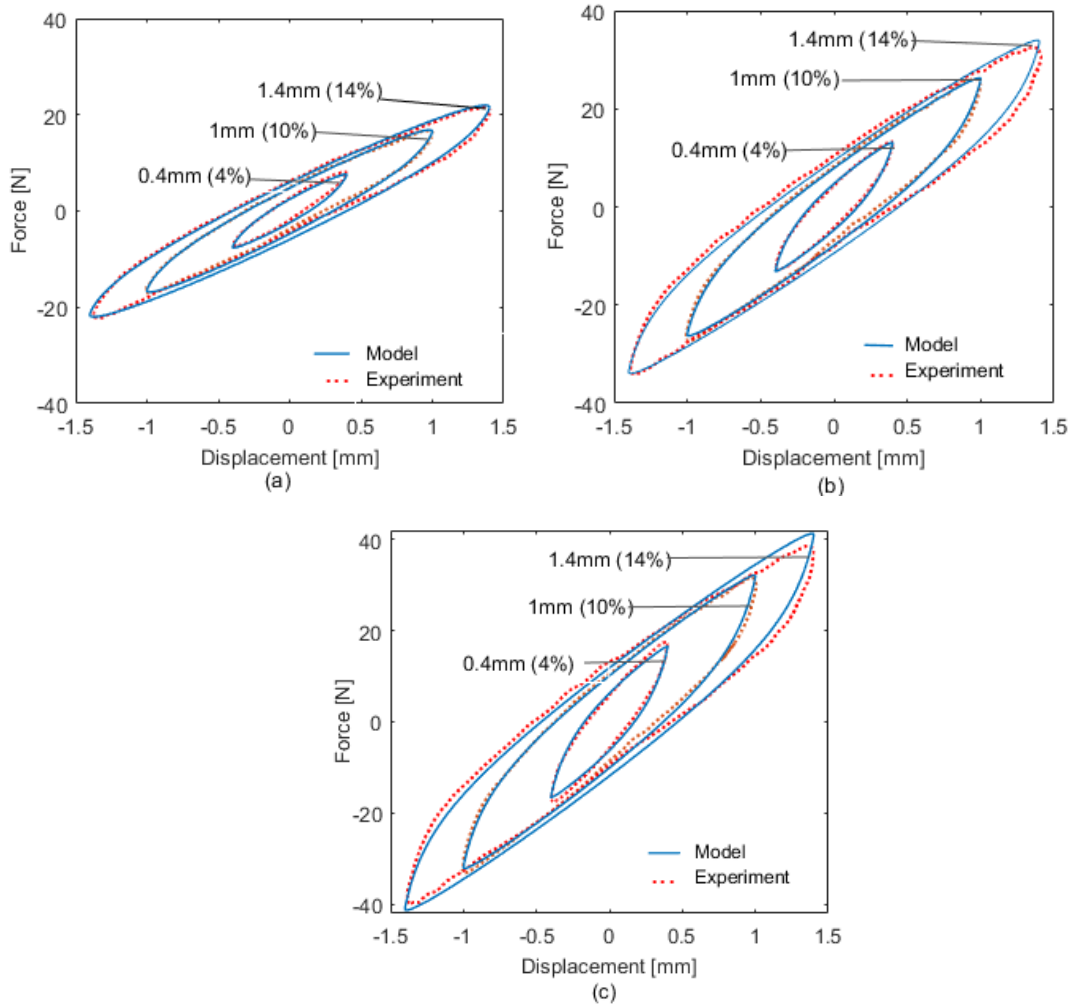
Figure 3.8 Force-displacement response under different amplitude levels with excitation frequency f =15 Hz: (a) $I = 0$ A (0 mT), (b) $I = 2$ A (218 mT), and (c) $I = 4$ A (267 mT).
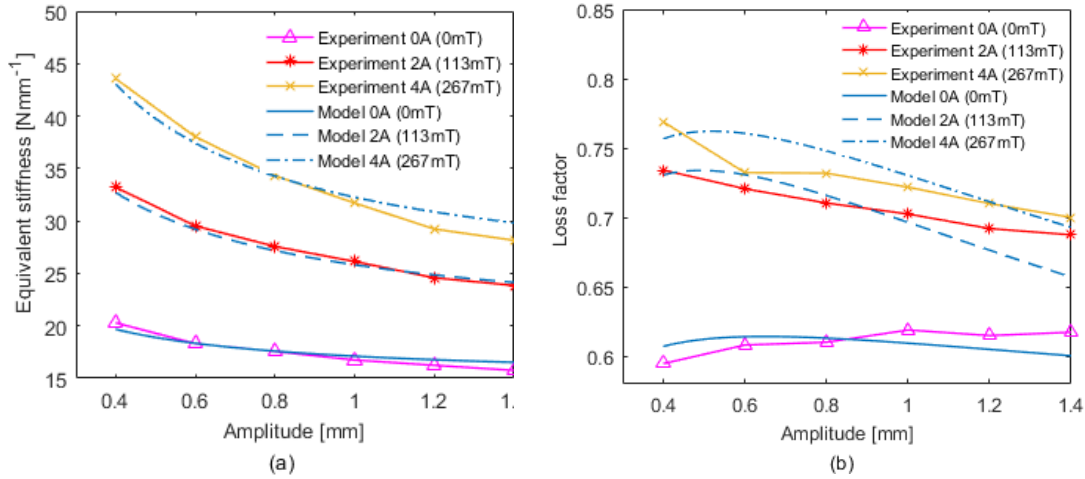
Figure 3.9 Stiffness and loss factor versus excitation amplitude for different levels of applied current with excitation frequency $f = 15$ Hz: (a) the equivalent stiffness and (b) the loss factor.
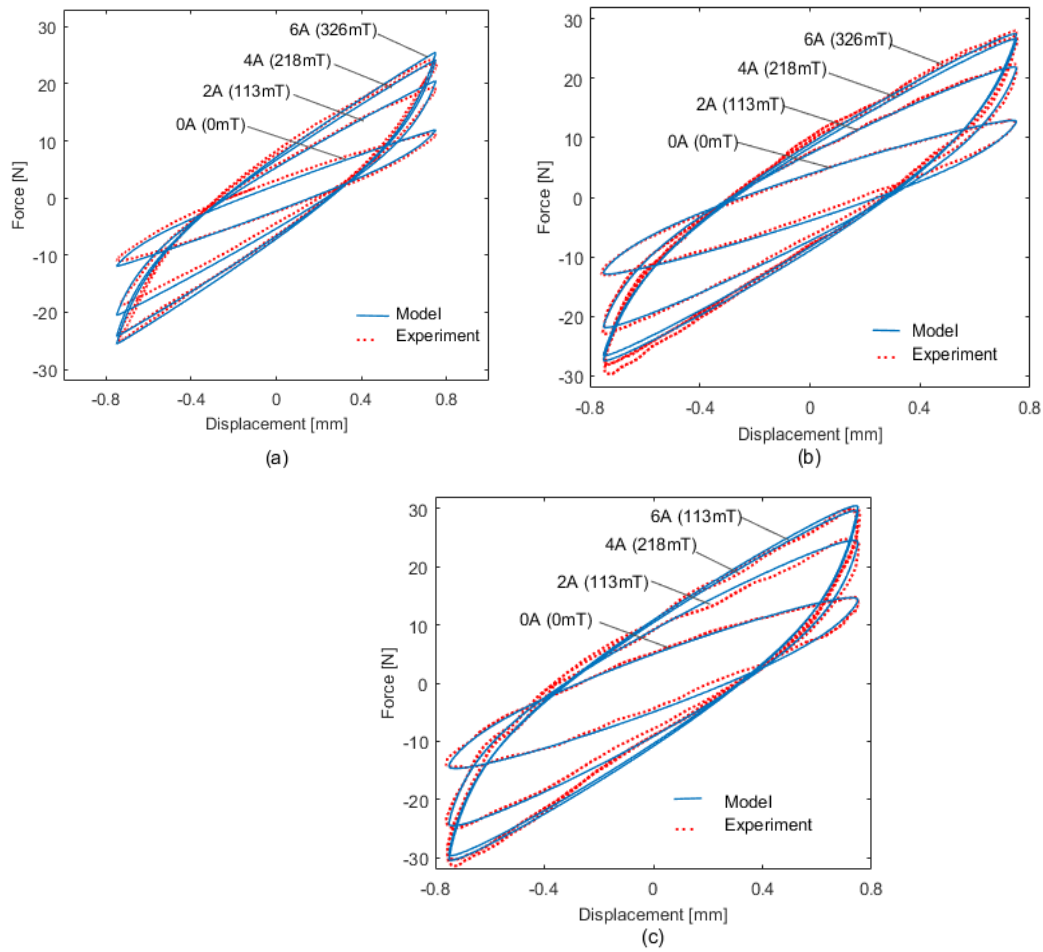
Figure 3.10 Force-displacement response under different levels of applied current with excitation amplitude $x_0 = 0.75\ mm$: (a) $f = 3$ Hz, (b) $f = 15$ Hz, and (c) $f = 30$ Hz.
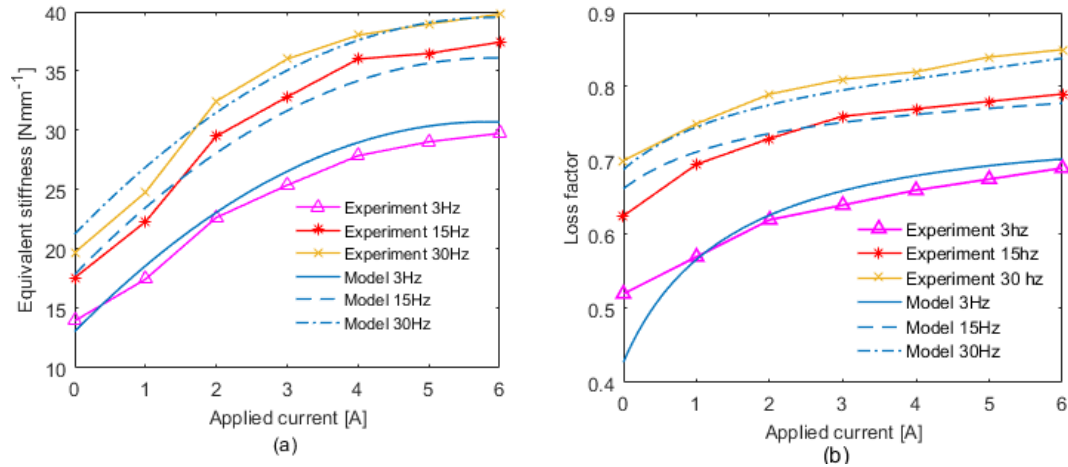
Figure 3.11 Stiffness and loss factor versus applied current for different frequencies with excitation amplitude $x_0 = 0.75$ mm: (a) the stiffness and (b) the loss factor.

Table 3.3 Fitness of the proposed model in frequency dependency (values are presented in percentage).

Frequency (Hz)	0 A	2 A	4 A	6 A
1 Hz	83.5	85.5	89.2	87.1
3 Hz	85.6	89.0	92.4	90.2
6 Hz	94.2	90.2	89.4	92.3
9 Hz	96.3	98.2	96.9	97.6
12 Hz	91.6	96.1	98.5	96.2
15 Hz	90.2	94.2	96.1	97.3
18 Hz	94.1	98.1	94.7	96.9
22 Hz	92.6	97.0	91.0	97.3
26 Hz	95.7	96.1	89.1	94.3
30 Hz	94.3	94.2	90.4	92.2

Table 3.4 Fitness of the proposed model in amplitude dependency (values are presented in percentage).

Amplitude (shear strain)	0 A	2 A	4 A	6 A
0.4 mm (4%)	85.1	91.0	91.1	89.3
0.6 mm (6%)	89.2	92.8	92.7	91.4
0.8 mm (8%)	92.9	93.4	94.0	94.2
1.0 mm (10%)	94.9	95.7	95.9	94.1
1.2 mm (12%)	95.4	96.5	95.6	95.6
1.4 mm (14%)	91.8	94.7	93.6	92.5

Table 3.5 Fitness of the proposed model in magnetic flux density dependency (values are presented in percentage).

Applied current (magnetic flux density)	1 Hz	9 Hz	18 Hz	30 Hz
0 A (0 mT)	83.5	97.3	94	94.1
1 A (59 mT)	86.1	96.6	94.3	93.4
2 A (113 mT)	85.2	98.2	98.1	94.2
3 A (167 mT)	87.4	96.4	95.2	92.7
4 A (218 mT)	89.2	96.9	94.7	90.4
5 A (267 mT)	90.5	96.7	96.1	93.1
6 A (316 mT)	87.1	97.3	96.9	92.7

3.5. Results and discussions

The proposed MRE model and relevant simulation results are compared with experimental results obtained by harmonic excitation. Three levels of displacement, three levels of input frequency, and four levels of magnetic field were arranged.

3.5.1 Frequency dependency

A displacement amplitude, $x_0 = 0.75$ mm, was set at excitation frequencies: f = 3, 15, and 30 Hz. Measurements were performed in three levels of magnetic field: 0 mT (0 A), 113 mT (2 A), and 218 mT (4 A). The force-displacement loops are shown in Figure 3.6. Overall agreement between measured and simulated loops is found. The loops tend to become elliptic as the frequency increases. The gradient of the main axis and the area of hysteresis loops become large as the external magnetic field increases. The smooth Coulomb friction model is adaptable in representing the rate-dependence of the force-displacement relationship. As shown in Figure 3.7, the equivalent stiffness and the loss factor defined by Eqs. (3.14) and (3.15) fit well with those from the measurements. Both the equivalent stiffness and the loss factor increase gradually by the increment of the excitation frequency. In addition, both values have similar trends for different levels of current.

3.5.2 Amplitude dependency

Under a harmonic excitation with frequency f =15 Hz, three displacement amplitudes were provided: x_0 = 0.4, 0.8, and 1.4 mm. Measurements and simulations were performed for three levels of magnetic field strength: 0 mT (0 A), 113 mT (2 A), and 218 mT (4 A). The force-displacement loops are compared in Figure 3.8. The force-displacement loops obtained by the numerical model agree well with the experimental result. The slopes of hysteresis loops decrease with the increase in amplitude and this trend is similar for all values of magnetic fields. As shown in Figure 3.9(a), the equivalent stiffness is well estimated by the proposed model. The stiffness decreases as excitation amplitude increases. The decreasing trend in

the loss factor obtained by the proposed model is found to coincide with the measured one at an acceptable level, as shown in Figure 3.9(b). The loss factor changes monotonically to the change in excitation amplitude. The similar trends are observed for all values of applied currents.

3.5.3 Magnetic field dependency

Under the displacement amplitude of $x_0 = 0.75$ mm, four levels of magnetic field were applied to the isolator: 0 mT (A), 113 mT (2 A), 218 mT (4 A), and 326 mT (6 A). The measurements and simulations were performed for three different excitation frequencies: 3 Hz, 15 Hz, and 30 Hz. The force-displacement loops are shown in Figure 3.10. A good agreement between measured and simulated loops can be found. The loops tend to become elliptic as the magnetic flux density increases. The difference between measured and simulated loops exhibits the same degree of error in different levels of magnetic flux density. Figure 3.11 shows the comparisons of equivalent stiffness and loss factor between proposed model and measured results. A good agreement between numerical responses and experimental results is achieved. The same tendency is observed with different excitation frequency; the higher the excitation frequency, the higher the equivalent stiffness and the loss factor became. Under specific excitation frequency, the equivalent stiffness shows parabolic increase as the applied current is increased. The loss factor increases gradually with the increase in applied current.

3.5.4 Fitness value of the proposed model

The fitness value is calculated by the following Eq. (20), using the normalized root mean square function [25].

$$Fitness value (\%) = 100 \times \left[1 - \frac{\left\| F_{Model} - F_{Exp} \right\|}{\left\| F_{Exp} - \overline{F}_{Exp} \right\|} \right], \qquad (3.20)$$

In Eq. (3.20), $\|...\|$ is the norm function, $\overline{...}$ the mean function (average value), F_{Model} the numerical force vector in one cycle, F_{Exp} the experimental force vector in one cycle. These vectors have the same displacement vector in response.

The calculated fitness values in percentage are listed in Tables 3.3, 3.4, and 3.5 for the respective dependency tests. In most cases, the fitness is higher than 90%. The average fitness is about 93%. From Tables 3.3 and 3.4, it is evident that the proposed model works effectively within the frequency range of 3 Hz and 30 Hz and shear strain between 6% and 14%. However, the model may provide inaccurate prediction results when working under low frequency and small amplitude excitation.

3.6 Summary

The dynamic viscoelastic model of the MRE-based isolator was presented, and a procedure to determine the six model parameters was introduced. The force-displacement relationship obtained by the numerical model is nearly consistent with the measurement results. Moreover, the proposed model predicts with high accuracy the dynamic viscoelastic characteristics of MRE in a wide range of frequencies (3–30 Hz) and shear strain (4%–16%). The MRE properties are strongly nonlinear functions of magnetic flux density, displacement amplitude, and the excitation frequency.

Chapter 4

Semi-active fuzzy control of 1-DOF system using magnetorheological elastomers

The MRE-based isolator is one of the semi-active devices that require an efficient controller. Because of nonlinearity in the model, not many control algorithms exist that could effectively operate MRE devices. The on-off algorithms are widely used include sky-hook on-off algorithm, clipped-optimal algorithm, Lyapunov algorithm, a sub-optimal H-∞ strategy [26-30]. In these algorithms, the command applied current has only two options: either zero or the maximum value. Consequently, fast switching produces periodical acceleration and jerk peaks that result in negative effects on the quality of structures.

In this chapter, the semi-active fuzzy vibration control with a strategy based on the Lyapunov theory and dynamic characteristic of MREs is developed for minimizing the movement of the isolator. Controller is expected to overcome the high acceleration and jerk peaks periodically of traditional semi-active controllers.

4.1 Dynamics model of 1-DOF system
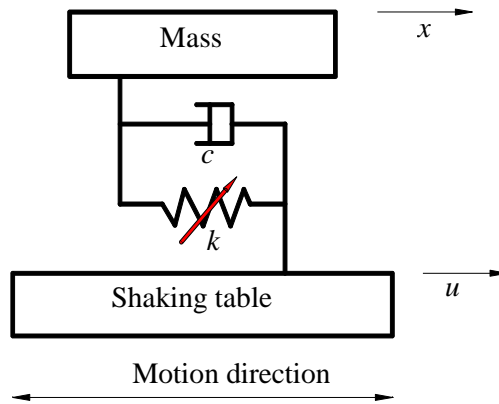
Figure 4.1 Base-excited 1-DOF system.

The mathematical model of a 1-DOF vibration system is shown in this subsection. The motion equation for the 1-DOF system shown in Figure 4.1 is described in time domain as

$$m\ddot{x} + c\dot{x} + k^*x = c\dot{u} + ku \tag{4.1}$$

In Eq. (4.1), x represents the displacement of mass m, u is the displacement of the ground base, c the MRE damping coefficient, $k^* = k_0 + \Delta k$ is the tunable MRE stiffness, k_0 is the minimum stiffness which is obtained without applied current, and Δk is the increment stiffness when the current is applied.

Transfer function $G(s)$ of the system in Laplace domain is defined as

$$G(s) = \frac{X(s)}{U(s)} = \frac{\dfrac{c}{k^*}s + 1}{\dfrac{m}{k^*}s^2 + \dfrac{c}{k^*}s + 1}. \tag{4.2}$$

In Eq. (4.2), $X(s)$ denotes the Laplace transform function of $x(t)$, and $U(s)$ is the Laplace transform function of $u(t)$.

Displacement transmissibility $T_R(\omega)$ of system $G(j\omega)$ is further defined by replacing s with $j\omega$ in the frequency response function $G(s)$, written as

$$T_R(\omega) = |G(j\omega)| = \sqrt{\frac{1 + (2\zeta\lambda)^2}{(1 - \lambda^2)^2 + (2\zeta\lambda)^2}}, \tag{4.3}$$

where $\lambda = \omega_0/\omega$, $\omega = \sqrt{k^*/m}$, $\zeta = c/2\sqrt{k^*m}$, ω_0 is the excitation frequency, ω is the tunable natural frequency of the isolation system, and λ, ζ are the dimensionless frequency and damping ratio, respectively.

MRE stiffness is found to increase steadily when the applied current changes from 0 A to 4 A, and achieve the saturation state when the applied current reach 4 A, as presented in chapter 3. The range of low to high stiffness was limited by the lower and upper bounds of the applied current, which correspond to 0 A and 4 A, respectively. Since the change of the damping coefficient in response to the applied current was insignificant, it is reasonable to assume that this coefficient is unchanged when applied current is varied.

4.2 Semi-active on-off vibration controller

A control strategy based on a robust, reliable control theory, namely, Lyapunov stability strategy, was applied. The dynamic equation for 1-DOF system (Eq. 4.1) can be rewritten as

$$m\ddot{x} + c(\dot{x} - \dot{u}) + k_0(x - u) = -\Delta k(x - u) \tag{4.4}$$

For the system given by Eq. (4.4), the Lyapunov function has the following form

$$V(x, \dot{x}) = \frac{1}{2}\left(\frac{k_0}{m}(x - u)^2 + \dot{x}^2\right) \tag{4.5}$$

Therefore, the derivative of the Lyapunov function associated with Eq. (4.4) can be derived as

$$\dot{V}(x, \dot{x}) = \frac{k_0}{m}(x - u)\dot{x} + \dot{x}\ddot{x}$$

$$= \frac{c}{m}(\dot{u} - \dot{x})\dot{x} - \frac{\Delta k}{m}(x - u)\dot{x}$$

$$= -\frac{c}{m}\dot{x}^2 - \frac{\Delta k}{m}(x - u)\dot{x} + \frac{c}{m}\dot{u}\dot{x} \tag{4.6}$$

The following on-off control algorithm to minimize the $\dot{V}(x, \dot{x})$ is proposed as

$$\Delta k = \begin{cases} 0 & (k^* = k_0, \ I = 0A) & \text{if} \ \ x_r\dot{x} < 0 \\ \Delta k_{max} & (k^* = k_{max}, \ I = I_{max}) & \text{if} \ \ x_r\dot{x} \geq 0 \end{cases} \tag{4.7}$$

In Eq. (4.7), k_0 and k_{max} signify the spring without applied current (I=0A) and with maximum applied current ($I = I_{max}$), $x_r = x - u$ is the relative displacement between the system mass and base, and $\dot{x}$ is the velocity of the system.

4.3 Semi-active fuzzy vibration controller
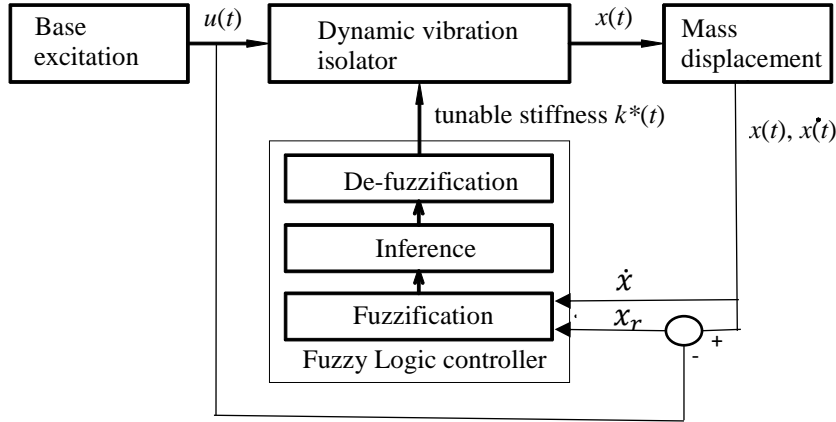
Figure 4.2 Block diagram of fuzzy logic controller for switching MRE stiffness.

In the on-off controller, the output choice is either off (0 A) or on (4 A). The fast switching of the on-off algorithm causes high acceleration and jerk peaks periodically, thus leading to the degeneration of the overall system quality. The problem can be resolved by using fuzzy logic to soften the fast switching action of the on-off control. The control system based on fuzzy logic control (FLC) analyzes analog input values in terms of logical variables.

As shown in Figure 4.2, the controller consists of three basic parts: fuzzification, where the continuous input variables are transformed into linguistic variables; fuzzy inference, which consists of fuzzy IF-THEN rules; and de-fuzzification, which interprets the values for the control variable. Relative displacement (x_r) and velocity ($\dot{x}$) were defined as the controller inputs and were divided into two intervals of linguistic

variables: negative (Neg) and positive (Pos). As the control output, tunable stiffness (k^*) was divided into high stiffness (High) and low stiffness (Low). The membership functions was depicted in Figure 4.3. Fuzzy rules play an important role in a fuzzy control system. The rules were based on the on-off semi-active algorithm (Eq. 4.7) and they were listed in Table 4.1 . The memberships were structured in the shape of a trapezoidal. The center of gravity method was adopted as the defuzzification to determine the command stiffness (k^*), which is widely utilized in fuzzy control systems for the Mamdani inference method.
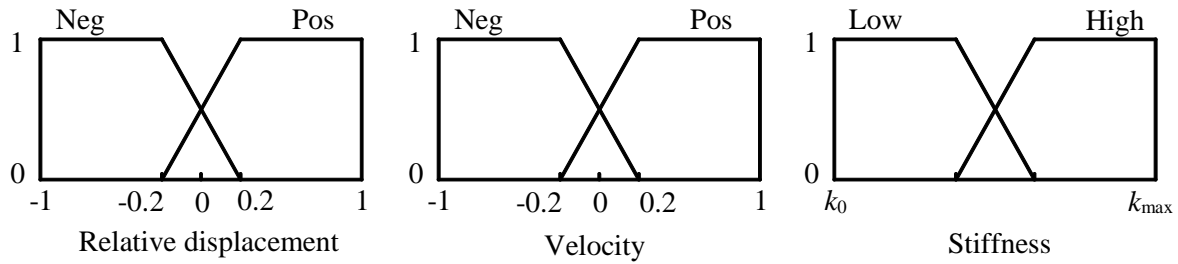
Figure 4.3 Fuzzy logic membership functions.

Table 4.1 Fuzzy logic rules.

Relative displacement/ Velocity	Neg	Pos
Neg	High	Low
Pos	Low	High
Fuzzy inference	Mamdani type	
De-fuzzification	Center of gravity	

Table 4.2 Parameters used in simulation.

Damping coefficient	1 Nsm^{-1}
Mass	1.138 kg
Spring constant (minimum, k_0)	974.5 Nm^{-1}
Spring constant (maximum, k_{max})	1948.9 Nm^{-1}
Base excitation amplitude	2 mm

4.4 Numerical evaluation for vibration control of 1-DOF system

System responses using passive, on-off semi-active, and fuzzy semi-active control schemes were calculated in order to evaluate the performance of the proposed controller. The model parameters are listed

in Table 4.2, where the actual value was used for the mass, whereas the damping coefficient was set lower than the actual value in order to emphasize the control effect.

The simulation results are shown in Figure 4.3 to 4.6 and listed in Table 4.3. Figure 4.3 shows the system frequency response. In this case, the frequency of the random base excitation varied between 1 Hz and 15 Hz. The figure shows that the displacement transmissibility was significantly reduced in both the on-off and fuzzy semi-active controls. An insignificant difference was found in the displacement transmissibility curves between these two control strategies. Figure 4.4 describes the displacement response of the mass under random excitation. Mass vibration was significantly suppressed by both the on-off and fuzzy semi-active controls. The on-off semi-active control performed slightly better than the fuzzy semi-active control.

The RMS and maximum values of the payload response are listed in Table 4.3. The values in parentheses represent the ratio of the values to those obtained for the passive-off case with minimum stiffness k_0. The RMS ratios of the displacement response in the fuzzy semi-active control decreased significantly to 0.45, whereas the values were 1 and 1.43 for the passive control with minimum and maximum stiffness, respectively. In addition, the acceleration RMS values also decreased in the case of the fuzzy semi-active control. The maximum displacement and acceleration responses when using the fuzzy semi-active control were much smaller than the response of the passive control cases. It is obvious that the energy consumption in the fuzzy semi-active control is much smaller than the energy required in the case of the passive-on control. The overall performance of the system that uses the fuzzy semi-active control surpassed that of the passive systems. The on-off semi-active system performed slightly better than the fuzzy semi-active system; the RMS ratios were 0.41 and 0.43 for the on-off and fuzzy controls, respectively. However, peak acceleration in the case of the on-off semi-active control was higher than in the case of the fuzzy semi-active control, as shown in Figure 4.5.

Figure 4.6 represents the required electric current for both the on-off and fuzzy semi-active controls. Based on the stiffness values k_0 and k_{max} obtained for the applied currents of 0 A and 4 A, the stiffness change within this range was assumed to be linear. The fast switching action of the crisp controller was softened by the fuzzy algorithm, and the current transition state became smoother. Consequently, the acceleration peaks were reduced when using the fuzzy algorithm. The figure shows that the fuzzy algorithm offered slight changes in the applied current at the frequent switching points of displacement (x) or velocity ($\dot{x}$), e.g., at points between 2.8 s to 3.2 s. In contrast, the on-off algorithm operated in high frequency. Furthermore, the actual current provided for the inductor requires transient time. Therefore, the fuzzy algorithm adapted more effectively to such current properties. It is demonstrated that the fuzzy semi-active

control system is effective in reducing structural responses, especially in the case of random excitations and high frequency.
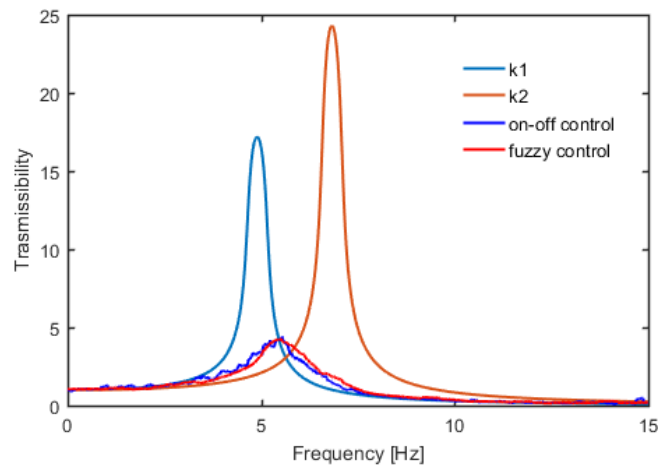

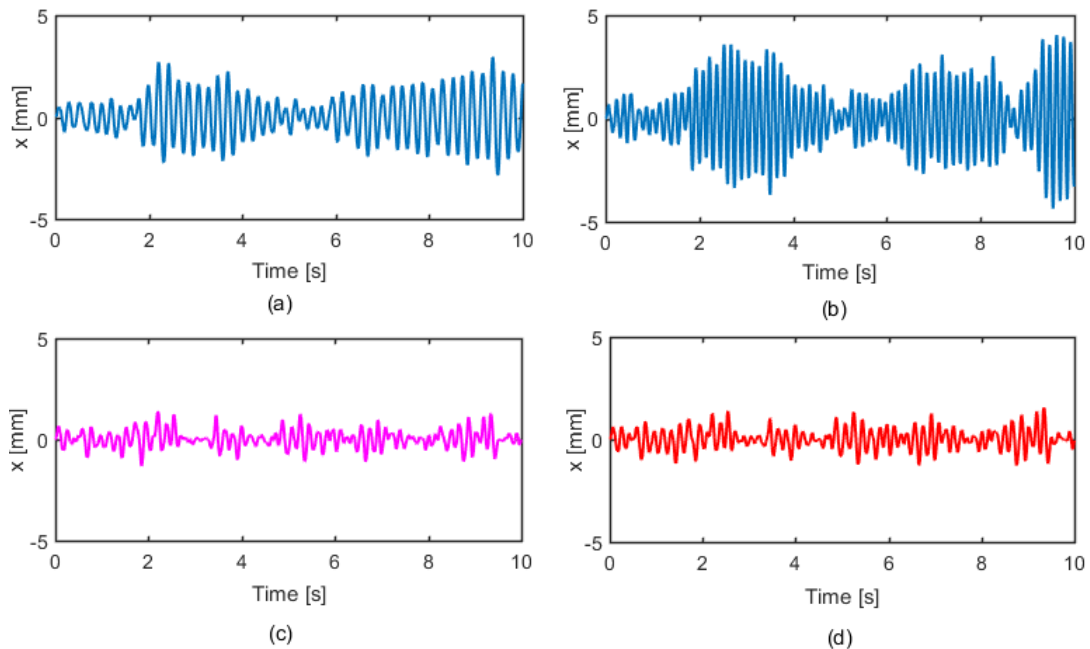Figure 4.3 Frequency response for 1-DOF system obtained by random excitation.

Figure 4.4 Displacement response by random excitation: (a) the passive ($k^* = k_0$), (b) the passive ($k^* = k_{max}$), (c) the on-off semi-active control, and (d) the fuzzy semi-active control.
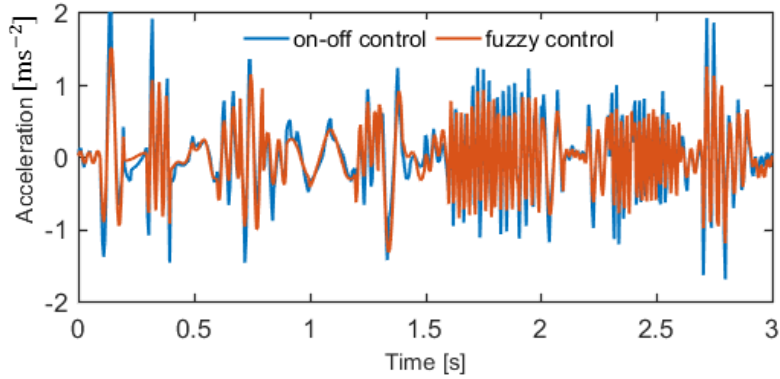
Figure 4.5 Acceleration response to random excitation for on-off semi-active control and for fuzzy semi-active control.
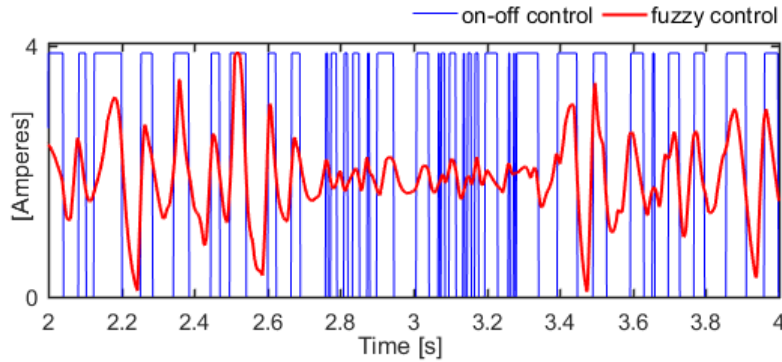
Figure 4.6 Applied current in on-off semi-active and fuzzy semi-active controls.

Table 4.3 Displacement and acceleration values of response to random excitation (simulation).

	RMS values		Maximum values	
	x [mm]	$\ddot{x}$[ms^{-2}]	x [mm]	$\ddot{x}$[ms^{-2}]
Passive-off (k_0)	1.07 (1)	0.99 (1)	2.95 (1)	2.62 (1)
Passive-on (k_{max})	1.53 (1.43)	2.71 (2.73)	4.04 (1.37)	8.5 (3.24)
On-off semi-active	0.44 (0.41)	0.75 (0.76)	1.38 (0.46)	2.99 (1.14)
Fuzzy semi-active	0.49 (0.43)	0.80 (0.78)	1.56 (0.53)	2.49 (0.85)

4.5 Experimental results

An experiment was conducted to assess the effectiveness of the MRE isolator using the experimental setup shown in Figure 4.7. A photo of the experimental apparatus is also shown in Figure 4.8. The parameters for experiment are listed in Table 4.4. In the experiment, the isolator that incorporated MRE with 40 vol% iron content was used. A pair of fabricated MRE samples was fixed between the iron cores

of the electromagnet as the variable spring. The lower core was fixed on the base, and the upper was allowed to move in the horizontal direction. The upper core and inductor were assumed to work together as the mass. Two laser displacement sensors were used to measure the displacements of the base and mass. The analog displacement signals were sent to a digital signal processor (TMS320C6713 DSK Board) controller as the input signals.

Figure 4.7 Experiment setup for MRE-based VI

(a)   (b)   (c)
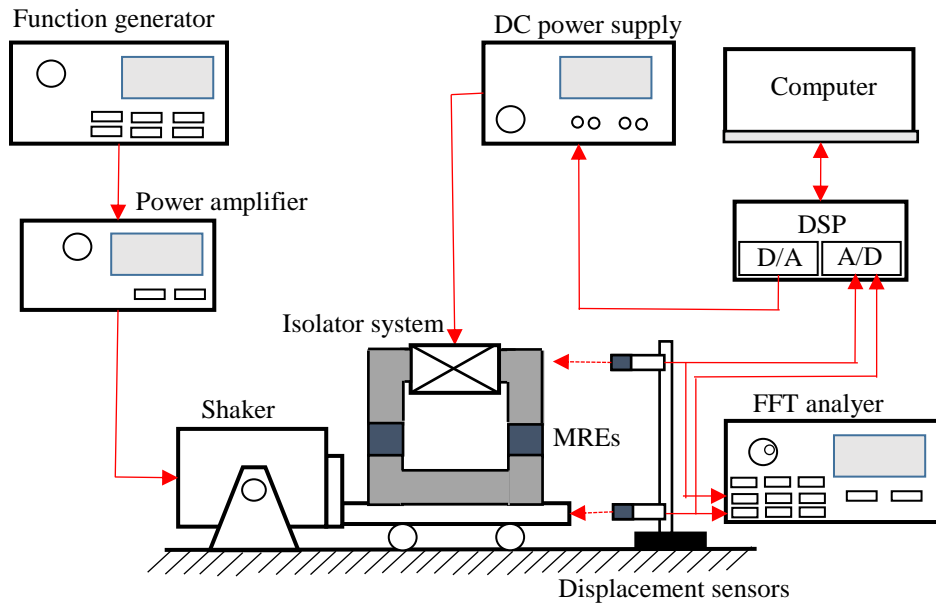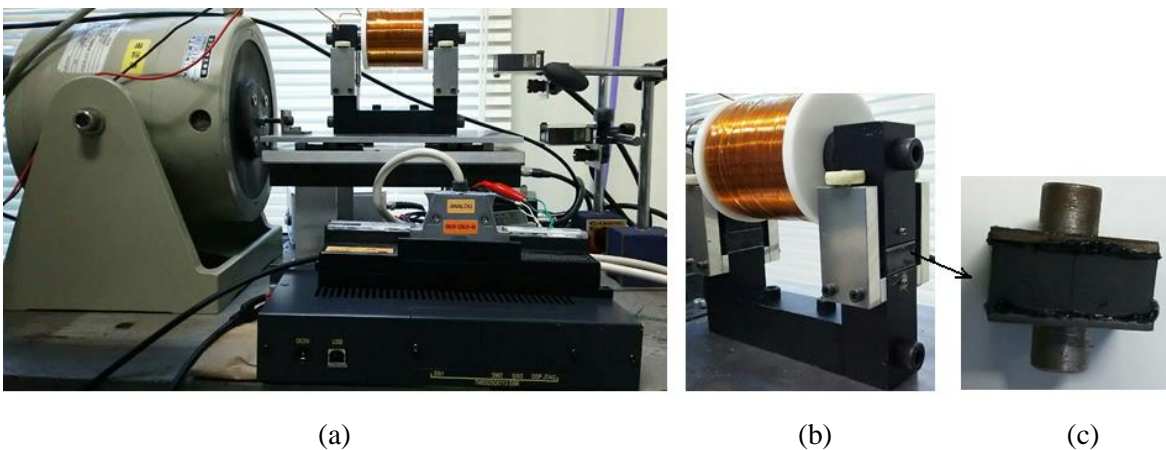
Figure 4.8 Photos for: (a) experiment setup, (b) isolator system, and (c) MRE sample.

Table 4.4 Parameters used in experiment.

MRE type	anisotropic MRE, 40 vol%
Number of MREs	2
Dimension of MREs	25x25x10 mm
Mass	1.138 kg
Minimum applied current	0 A
Maximum applied current	4 A
Frequency excitation	1-50 Hz
Base excitation amplitude	1 mm
Excitation type	random

Based on the control algorithms defined by Eq. (4.7) for the on-off algorithm and Table 4.1 for the fuzzy rules, the output signal was calculated and sent to the direct current (DC) power supply to drive the inductor. The base excitation was induced by the exciter driven by the power amplifier, and the power amplifier received the base excitation signal from the function generator.

The experimental results are shown in Figures 4.9 and 4.10, and listed in Table 4.5. Figure 4.9 shows the displacement transmissibility curves for the white-noise random excitation of the cutoff frequency 50 Hz. The results were compared among three passive systems (the constant applied current values were 0A, 2A, and 4A, respectively), and two semi-actively controlled systems that used the two types of controller described previously. The transmissibility was small and almost the same when the systems worked in the high-frequency region (over 30 Hz). In contrast, the transmissibility was high and different for the different control strategies in the low-frequency region. The passive system with zero applied current had the smallest natural frequency and highest peak of transmissibility. The passive system with 4A-applied current had the largest natural frequency and lowest peak of transmissibility. These results are consistent with the MRE material properties mentioned in chapter 3: the stiffness and loss damping coefficient for MRE increased when the applied current increased accordingly. Noticeably, transmissibly was reduced significantly in the low frequency when the semi-active controllers were used. The performance was found to be more effective in the case of using the fuzzy algorithm than in the case of using the on-off algorithm.

Figure 4.10 shows the displacement response of the mass under different control strategies. The mass vibration was remarkably suppressed when the semi-active control algorithms were applied. The fuzzy algorithm worked better than the on-off algorithm. The RMS and maximum values of the mass are listed in Table 4.5, both values were reduced significantly using these controllers. The fuzzy control performed better than the on-off control. The reduction rates were 31% and 34% for the RMS and maximum displacement values, respectively. The acceleration RMS and maximum acceleration values also decreased in the case of the fuzzy semi-active control by 21% and 37%, respectively.

From Figures 4.5, 4.5, 4.6 (simulated results) and Figures 4.9, 4.10 (experimental results), the effectiveness of Fuzzy semi-active strategy can be explained by its operation mechanism. MRE-based isolator is used to produce external force ($F = x_r \times \Delta k$) on structure in order to absorb vibration energy in response to a desirable applied current. In the case of large displacement, if the system tends to leave the equilibrium position ($x_r \dot{x} < 0$), both the isolator with on-off semi-active controller and the isolator with fuzzy semi-active controller operate with the same mechanism. These isolators produce maximum force ($F = \Delta k_{max} x_r$) to absorb vibration as much as possible. The effectiveness of these two controllers is the same in this situation. In contrast, if the system tends to return to the equilibrium position ($x_r \dot{x} \geq 0$), the isolator with on-off semi-active controller does not produce external force ($F = 0, I = 0$), then the system returns to equilibrium position freely. Consequently, the system will overshoot out of equilibrium position because of system inertia, especially in the case of high acceleration. The isolator with fuzzy semi-active control produces a sufficient force to restrict this overshoot. This sufficient force depends on fuzzification and inference processing based on human knowledges, experiences and observations in many cases of studies. As a result, fuzzy algorithm is more effective than on-off algorithm in this situation, and it helps structure reaching nearly their critically damped point. In the case of small displacement, the isolator with on-off controller produces either maximum or minimum force around equilibrium, which causes chattering or an underdamped vibration. However, the isolator with fuzzy semi-active controller produces a sufficient force. Consequently, Fuzzy strategy is also more effective in this case.
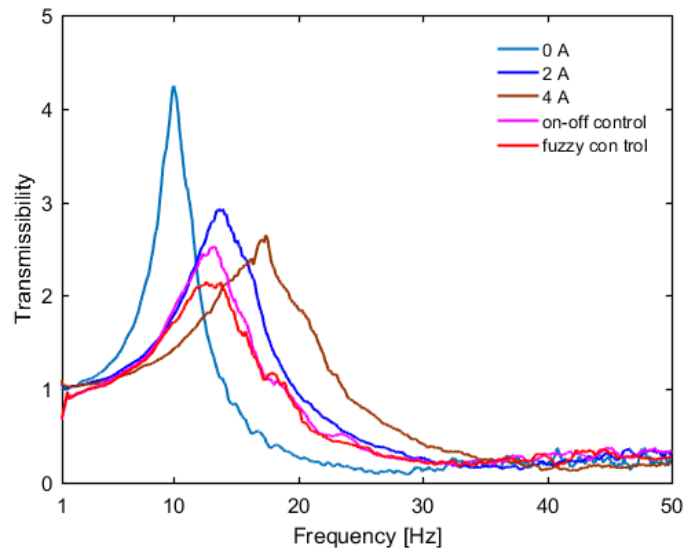

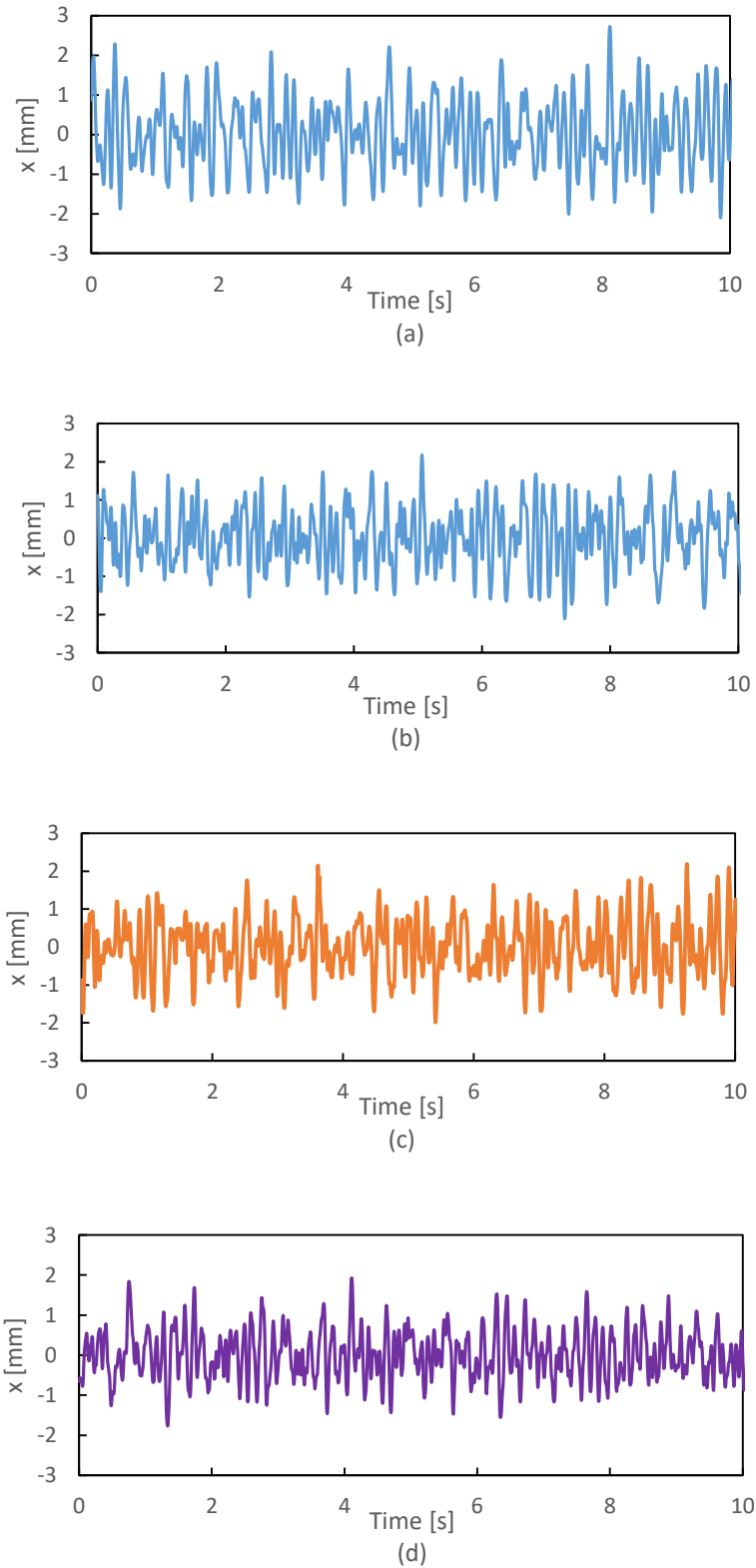Figure 4.9 Frequency response by random excitation (experiment).

Figure 4.10 Displacement response to random excitation (experiment): (a) passive-off (0 A), (b) passive-on (4 A), (c) the on-off semi-active control, and (d) the fuzzy semi-active control.

Chapter 4: Semi-active fuzzy control of 1-DOF system using MREs

Table 4.5 Displacement and acceleration values of response to random excitation (experiment).

	RMS values		Maximum values	
	x [mm]	$\ddot{x}$[ms^{-2}]	x [mm]	$\ddot{x}$[ms^{-2}]
Passive-off (I=0A)	1.08 (1)	1.03(1)	3.4 (1)	6.24(1)
Passive-on (I=4A)	0.96 (0.88)	1.26(1.22)	3.18 (0.93)	4.98(0.79)
On-off semi-active	0.85 (0.78)	0.92(0.89)	2.6 (0.76)	4.52(0.72)
Fuzzy semi-active	0.75 (0.69)	0.82(0.79)	2.26 (0.66)	3.95(0.63)

4.6 Summary

The stiffness was controlled by controlling electric current applied to an electromagnet. The fuzzy algorithm was developed with the aim of switching MRE stiffness smoothly in comparison with the on-off type algorithm. The real-time vibration control performance of the semi-active fuzzy isolator system was evaluated by both computer simulation and experiment for a single DOF system. The performance was compared with that of passive systems and a system with on-off type controller. The results showed that the semi-active fuzzy control provided better performance than its counterparts, not only by reducing chatter, but also conserving the electrical energy of the device. When tuned appropriately, the semi-active fuzzy controller is capable of improving the response characteristics and efficiency of semi-active type systems.

Chapter 5

Semi-active fuzzy control of multi-degree-of-freedom structure using magnetorheological elastomers

In this chapter, a semi-active fuzzy controller was designed to enhance the performance of the isolator in suppressing multi-degree-of-freedom structural vibrations. The control strategy was built to determine the command applied current. The controller is completely adequate for handling the nonlinearity of the isolator and works independently with the building structure. The efficiency of the MRE-based isolator was evaluated by the responses of the scaled building under seismic excitation. Numerical and experimental results show that the isolator accompanied with a fuzzy controller remarkably reduces the relative displacement and absolute acceleration of the scaled building compared to passive-off and passive-on cases.
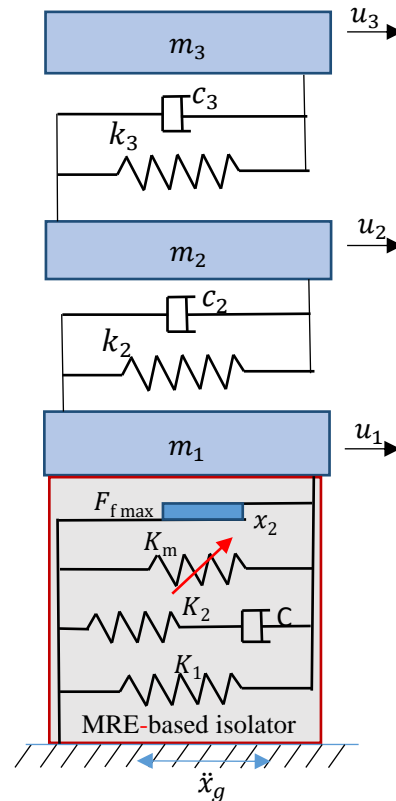

Figure 5.1 Schematic of the two-story building with a fundament plate is rigidly connected by an MRE-based isolator.

Table 5.1 Scaling factor of the variables

Variables	Height	time	frequency	acceleration	mass
Scaling factor	1:25	1:5	5:1	1:1	1:625

5.1 A model of the isolated building

In order to evaluate the performance of MRE-based isolator, a two-story building structure (m_2, m_3) with a fundament plate (m_1) which is rigidly connected to the isolator is considered as shown in Figure 5.1. The isolator is also connected rigidly to the ground.

The equation of motion can be written as follows,

$$M\ddot{u} + C\dot{u} + Ku = \Lambda f_{MRE} - M\Gamma\ddot{x}_g. \tag{5.1}$$

In Eq. (5.1), M, C, and K represent $(n \times n)$ mass, damping, and stiffness matrices, respectively; $u = [u_1 \quad u_2 \quad u_3]^T$ is the vector of the displacements of the masses relative to the ground; f_{MRE} is the control force generated by an MRE-based isolator; $\ddot{x}_g$ is ground acceleration; $\Lambda = [1 \quad 0 \quad 0]^T$ is the matrix determined by the placement of control devices; Γ is the column vector of ones. The mass of the floors are $m_1 = 3$ kg, and $m_2 = m_3 = 2$ kg. The stiffness and damping are determined from the real structure as $k_2 = k_3 = 1.1 \times 10^5$ N m^{-1} and $c_2 = c_3 = 2$ N s m^{-1}, respectively. The system matrices of a two-story shear building with a fundament plate are,

$$M = \begin{bmatrix} m_1 & 0 & 0 \\ 0 & m_2 & 0 \\ 0 & 0 & m_3 \end{bmatrix}, C = \begin{bmatrix} c_2 & -c_2 & 0 \\ -c_2 & c_2 + c_3 & -c_3 \\ 0 & -c_3 & c_3 \end{bmatrix}, K = \begin{bmatrix} k_2 & -k_2 & 0 \\ -k_2 & k_2 + k_3 & -k_3 \\ 0 & -k_3 & k_3 \end{bmatrix}.$$

Defining the state vectors as $z = [u \quad \dot{u}]^T$, Eq. (5.1) can be written in state space form as follows,

$$\dot{z} = Az + Bf_{MRE} + E\ddot{x}_g, \tag{5.2}$$

where, $A = \begin{bmatrix} 0 & I \\ -M^{-1}K & -M^{-1}C \end{bmatrix}, B = \begin{bmatrix} 0 \\ M^{-1}\Lambda \end{bmatrix}, E = \begin{bmatrix} 0 \\ -\Gamma \end{bmatrix}.$

The two-story building model is investigated with height scale factor of 1:25. The height of the model is 0.3 m that corresponds to a height of 7.5 m of the real two-story building. All variables and dimensions are scaled according to modeling laws [18], and their values are summarized in Table 5.1. Four cases were investigated in both numerical evaluation and experiment: "fixed base" means that the building is fixed to the ground (2DOF); "passive off" means the isolated building that works with an isolator without applied current (0 A); "passive on" means the isolated building that works with an isolator applied by a current (5 A); "fuzzy control" means the isolated building that works with an isolator controlled by fuzzy algorithm.

5.2 Semi-active fuzzy control

The fuzzy logic controller is designed to determine the command applied current of the MRE-based isolator according to its relative velocity and relative displacement. The isolator regulates the viscoelastic force according to the applied current input. The block diagram of the controller is shown in Figure 5.2.
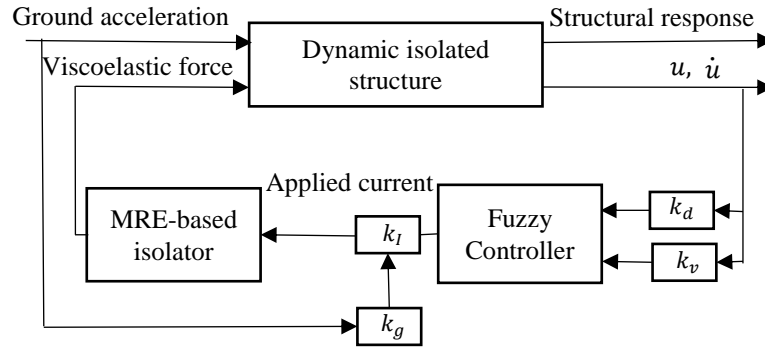
Figure 5.2 Fuzzy control system
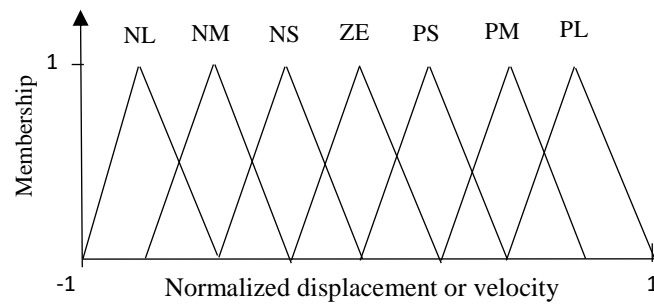
Figure 5.3 Input membership functions
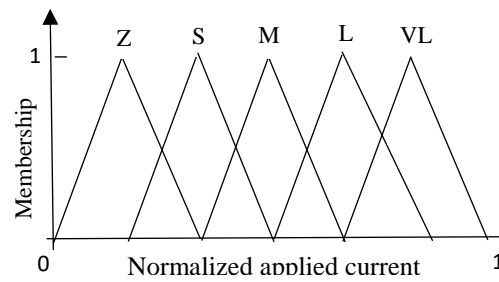
Figure 5.4 Output membership functions

Table 5.2 Fuzzy inference rule

$\dot{u}$ \ u	NL	NM	NS	ZE	PS	PM	PL
NL	VL	VL	L	L	M	S	ZE
NM	VL	VL	L	M	S	ZE	S
NS	VL	L	M	S	ZE	S	M
ZE	L	M	S	ZE	S	M	L
PS	M	S	ZE	S	M	L	VL
PM	S	ZE	S	M	L	VL	VL
PL	ZE	S	M	L	L	VL	VL

The relative displacement and relative velocity of the fundament plate to the ground are selected as two input variables (Figure 5.3), and command applied current is employed as a single output variable (Figure 5.4). The definitions of the membership function of input variables are as follows: negative large (NL); negative medium (NM); negative small (NS); zero (ZE); positive small (PS); positive medium (PM); positive large (PL). For the electric current output, the control output functions are as follows: zero (ZE); small (S); medium (M); large (L); and very large (VL). The membership functions are structured in the shape of a triangle with Mamdani-type inference system; the center of gravity method is used for de-fuzzification. The rules are based on the skyhook on/off algorithm shown in Table 5.2.

The fuzzification factors used to convert the inputs into fuzzy variables are defined as k_d and k_v, for the relative displacement and the relative velocity, respectively. The de-fuzzification factor used to convert the output is k_I. From the best results among considerable cases studied, k_I seems to be strongly related to the ground acceleration.
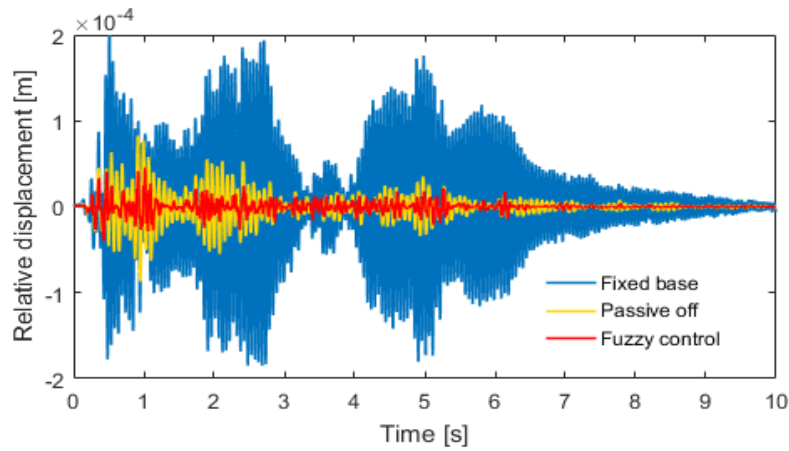
(a)
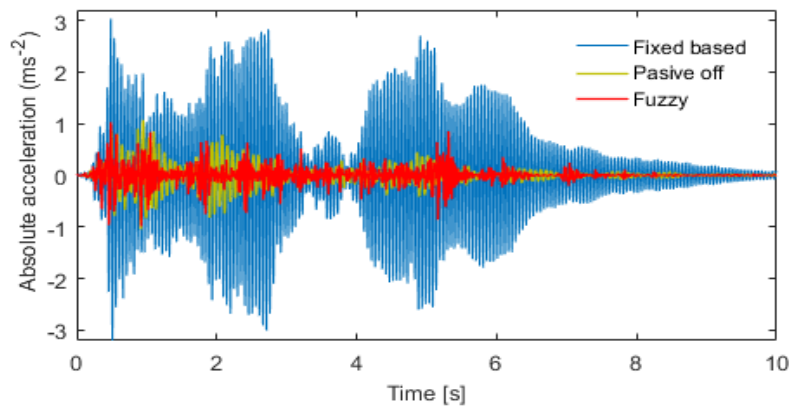
(b)

Figure 5.5 The relative displacement and absolute acceleration responses under El Centro earthquake: (a) the relative displacement response of the third mass to the fundament plate (the first mass), and (b) the absolute acceleration response in the third mass.
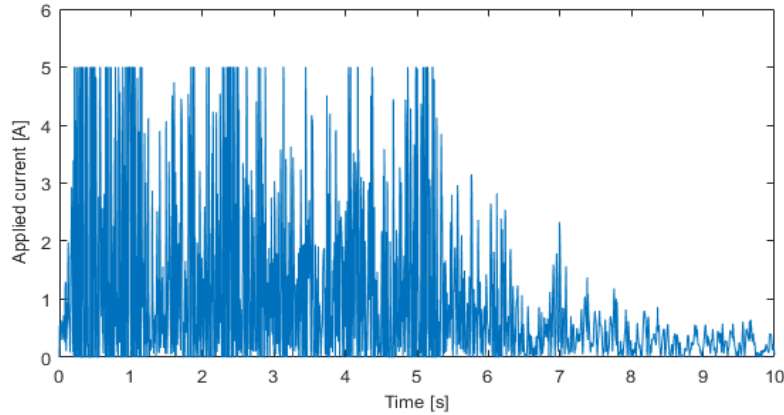
Fig. 5.6 Applied current for MRE-based isolator under El Centro earthquake

Table 5.3 Evaluated performance indices due to El Centro earthquake (RMS: root mean square; disp.: relative displacement of the third mass to fundament plate; acc.: absolute acceleration of the third mass).

Control strategy	RMS disp. (mm)	Max. disp. (mm)	RMS acc. (ms^{-2})	Max. acc. (ms^{-2})
Fixed based	0.062 (1)	0.21 (1)	0.94 (1)	3.03 (1)
Passive-off	0.017 (0.27)	0.075 (0.36)	0.21 (0.22)	1.07 (0.35)
Passive-on	0.011 (0.18)	0.06 (0.28)	0.31 (0.32)	1.2 (0.39)
Fuzzy	0.009 (0.15)	0.05 (0.24)	0.18 (0.17)	1.02 (0.33)

5.3 Numerical evaluation of the control performance

The performances of the "fixed base," "passive off," and "fuzzy control" are compared for the scaled El Centro earthquake. The responses of the scaled building to the scaled earthquake are shown in Figures 5.5, 5.6 and Table 5.3. The relative displacement response of the third mass to the fundament plate is significantly reduced in the case of the isolated building in comparison to the "fixed base" (Fig. 5.5a). The "fuzzy control" performs remarkably better than the "passive off." In particular, the third mass absolute acceleration response is significantly suppressed in the system with MRE-based isolator (Fig. 5.5(b)). The "fuzzy control" performs moderately better than the "passive off" case in reducing the acceleration response. Figure 5.6 shows the command applied current supplied to the MRE-based isolator with fuzzy controller. In the case of large displacement, the current supplied to the isolator switches between 0 A and 5 A. In the case of small displacement, the fuzzy controller produces a sufficiently necessary applied current for control. Time integral of the applied current signal indicates that the energy consumption in the "fuzzy control" is reduced by 65% in comparison to the energy required in the case of "passive on."

The RMS and maximum values of the third mass response are listed in Table 5.3. The values in parentheses represent the ratio of the values to those obtained for the fixed building. The RMS ratio of the relative displacement response of third mass to the fundament plate in the case of "fuzzy control" is

significantly reduced to 0.15 for the El Centro earthquake. The absolute acceleration RMS values of third mass are also decreased. In addition, the ratio of the maximum relative displacement and absolute acceleration response decrease to 0.24 and 0.33; all tested cases have minimum values.

5.4 Experimental results

Figure 5.7 shows a photo of a scaled building (1:25). The displacement sensors and accelerometers are installed and calibrated on each floor of the scale building and shaking table. The analog displacement signals are sent to a digital signal processor (TMS 320 C6713 DSK Board). The fuzzy algorithm explained in section 5.2 is embedded in this processor to determine the command applied current. A high speed bipolar power supply (Matsusada Precision Inc., Series POP 65-5) is used for the experiments such that the actual current precisely tracks the command current for the MRE-based isolator in real time. The swept-sine and random excitation were used to excite the table.
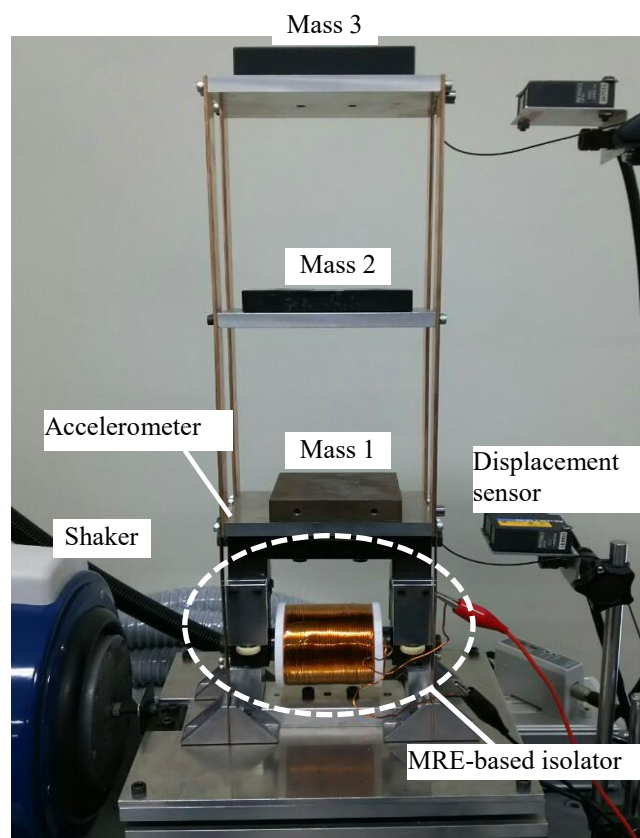

Figure 5.7 Experimental setup: The building consist of two story (corresponding mass 2 and mass 3) and the MRE-based isolator is connected to the building model by the fundament plate (mass 1).

The experimental results are shown in Figures 5.8-5.12 and Tables 5.4 and 5.5. Figure 5.8 shows the displacement and acceleration transmissibility of the third mass responding to swept-sine excitation. The transmissibility is reduced significantly in the isolated building. The first natural frequency of the isolated building shifts from 7.6 Hz to 10.1 Hz. Furthermore, the efficiency of isolation is improved using a fuzzy controller.

The maximum displacements and absolute accelerations are shown in Figure 5.9. In "fuzzy control," the maximum displacement and the absolute acceleration of superstructure are decreased. Particularly, Figure 5.10 shows the maximum values of the relative displacement. Better performances can be found in the isolated building than in the case of the fixed building. The isolator with fuzzy controller achieves the best performance. In Tables 5.3 and 5.4, numbers in parentheses denote the ratio of peak response and root mean square (RMS) values of the structure to those obtained for "fixed base" case. The peaks of the third mass displacement relative to the ground (u_3) and the absolute acceleration ($\ddot{u}_3$) are reduced by 15% and 24% respectively in "fuzzy control" compared to the "fixed base." The maximum relative displacement (u_3 - u_1) also decreases by 30% for "fuzzy control." Moreover, the root mean square (RMS) values also reduce holistically for the structure equipped with the isolator with fuzzy controller.

Figure 5.11 shows time histories of the third mass absolute acceleration response; Figure 5.12 shows the histories of the relative displacement response of the third mass to the fundament plate. It is evident that the responses are remarkably suppressed in the case of "fuzzy control." These responses significantly affect the destruction of the system under seismic events. Therefore, the application of MRE-based isolator with fuzzy controller is a promising measure to protect the building from collapse or fracture.

(a)   (b)
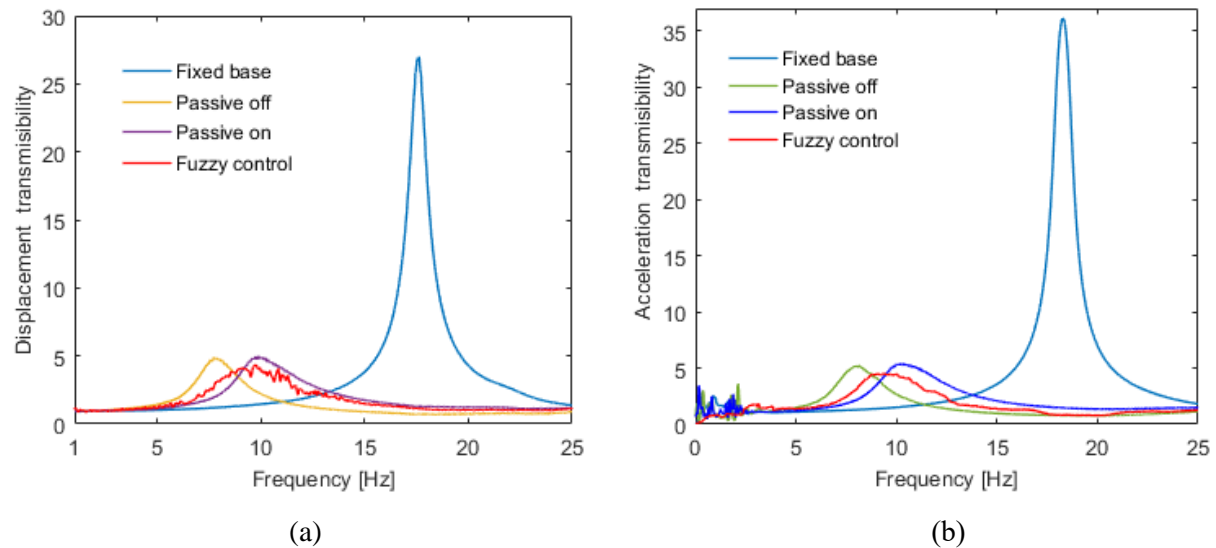
Figure 5.8 Transmissibility of the scaled building: (a) displacement transmissibility and (b) acceleration transmissibility.

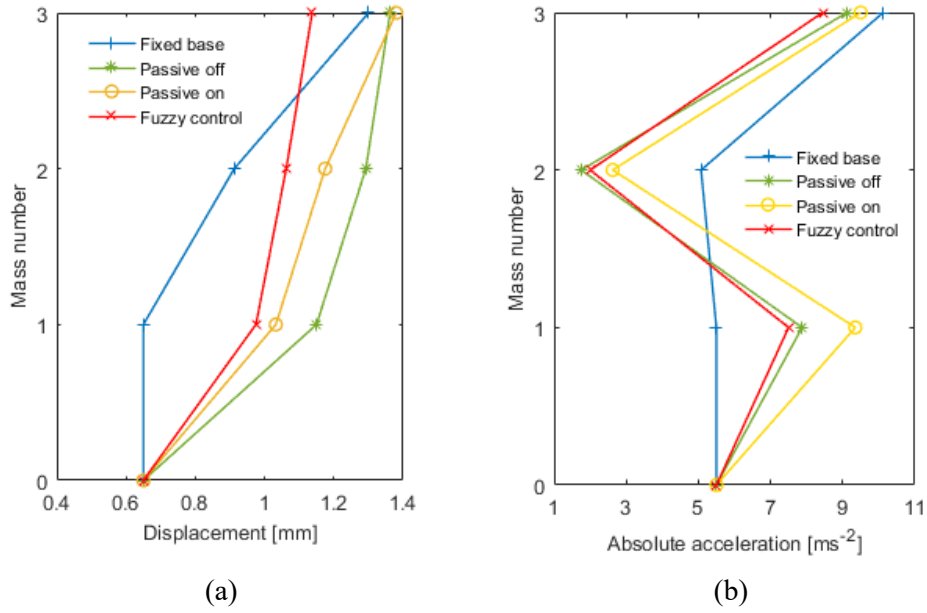(a)   (b)

Figure 5.9 Maximum displacement and absolute acceleration of scaled building: (a) displacement and (b) absolute acceleration.
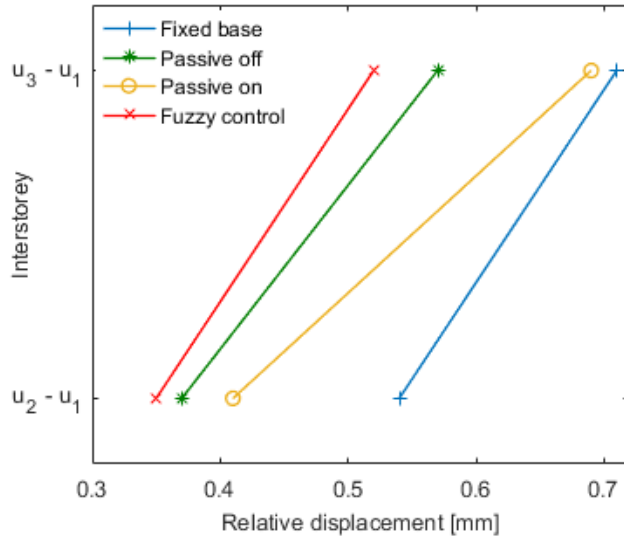
Figure 5.10 Maximum values of relative displacement.
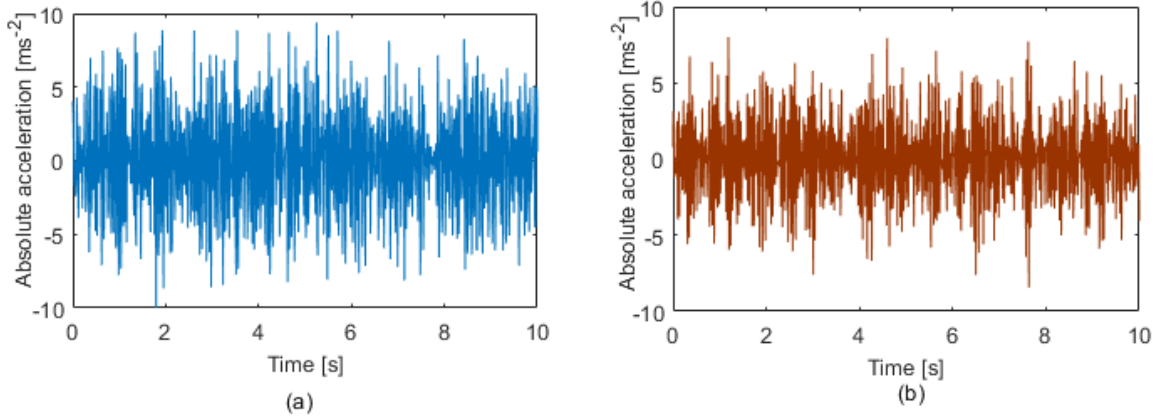
Figure 5.11 The absolute acceleration of the third mass: (a) fixed base and (b) fuzzy control.
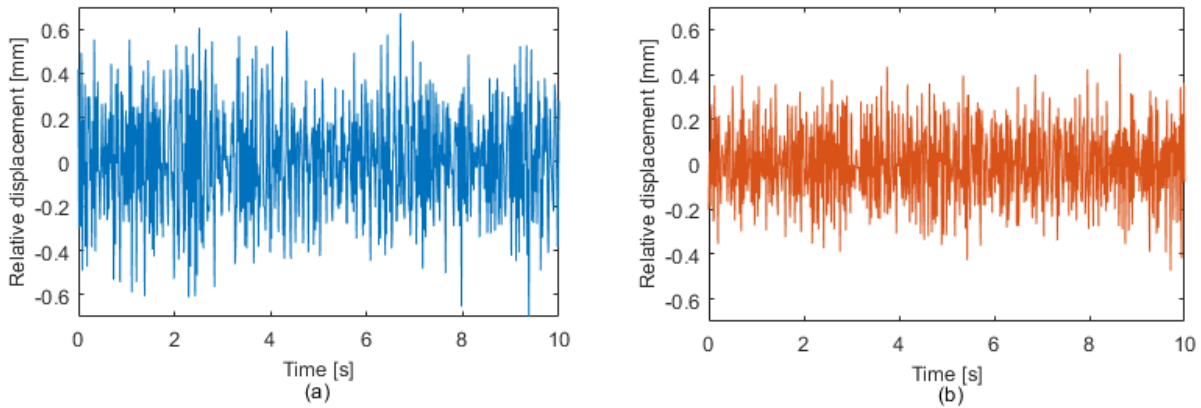
Figure 5.12 The relative displacement of the third mass to the fundament plate (first mass): (a) fixed base and (b) fuzzy control.

Table 5.3 Peak displacement of the third mass to the ground (u_3), peak absolute acceleration of the third mass ($\ddot{u}_3$), and peak relative displacement ($u_3 - u_1$) obtained in random excitation. Numbers in parentheses represent the ratio of peak value to that obtained in the case of "Fixed base."

Control strategy	Fixed base	Passive off	Passive on	Fuzzy control
u_3 (mm)	1.30 (1)	1.36 (1.05)	1.38 (1.06)	1.11 (0.85)
$\ddot{u}_3$ (ms^{-2})	11.10 (1)	9.12 (0.82)	9.50 (0.85)	8.45 (0.76)
$u_3 - u_1$ (mm)	0.67 (1)	0.57 (0.85)	0.71 (1.05)	0.47 (0.70)

Table 5.4 Root mean square (RMS) displacement of the third mass to the ground (u_3), RMS absolute acceleration of the third mass ($\ddot{u}_3$), and RMS relative displacement ($u_3 - u_1$) obtained in random excitation. Numbers in parentheses represent the ratio of RMS value to that obtained in the case of "Fixed base."

Control strategy	Fixed base	Passive off	Passive on	Fuzzy control
u_3 (mm)	0.45 (1)	0.41 (0.91)	0.40 (0.88)	0.38 (0.84)
$\ddot{u}_3$ (ms^{-2})	3.51 (1)	2.90 (0.82)	3.03 (0.86)	2.85 (0.81)
$u_3 - u_1$ (mm)	0.21 (1)	0.19 (0.90)	0.23 (1.09)	0.169 (0.80)

5.5 Summary

Vibration responses of a scaled two story building were investigated. Using MRE-based isolator, the transmissibility of the building is reduced significantly and the first natural frequency shifts from 7.6 Hz to 10.1 Hz by switching applied current. A fuzzy control algorithm was used to enhance performance of the MRE-based isolator. Both numerical simulation and experimental results show that the "fuzzy control" provides better performance than "fixed base," "passive off," and "passive on." The peaks of the third mass displacement and absolute acceleration are reduced by 15% and 24%, respectively. The maximum relative displacement between third mass and fundament plate also decreases by 30%. The MRE-based isolator used in conjunction with the fuzzy controller is efficient for mitigating vibrations in a two story building.

Chapter 6

Robust adaptive controller for semi-active control of uncertain structures using an MRE-based isolator

In this chapter, the design of the new semi-active controller for an MRE-based isolator is investigated to overcome the drawbacks of traditional controllers from two perspectives. Firstly, an inverse model is designed for the isolator so that it can be used to predict an appropriate electric current supplied to the electromagnet based on the desired control force. Secondly, a robust adaptive controller is proposed for a nonlinear system with unknown dynamic parameters. The control scheme consists of three parts: a standard adaptive linearizing controller, an adaptive sliding mode controller, and a single robust controller. The proposed method guarantees zero convergence of the displacement response and provides robust stability. In addition, the singularity problem that usually appears in standard adaptive control is eliminated. Simulations demonstrate that the proposed controller exceeds the performance of the passive system as assessed in the protection of a two-story shear building during seismic events.

6.1 Limitations on force generation of the MRE-based isolator

In active control, the control force can be generated at any value and direction of the force. However, in the MRE-based isolator, the force of the isolator is determined by $F = k^* x$, (where k* >0 is the variable stiffness, and x is the displacement). Therefore the force can be generated at variable value but the same direction with displacement, as schematically shown in Figure 6.1(a). The criterion for the force, $F(t)$, generated by the MRE-based isolator, can be described as follows.
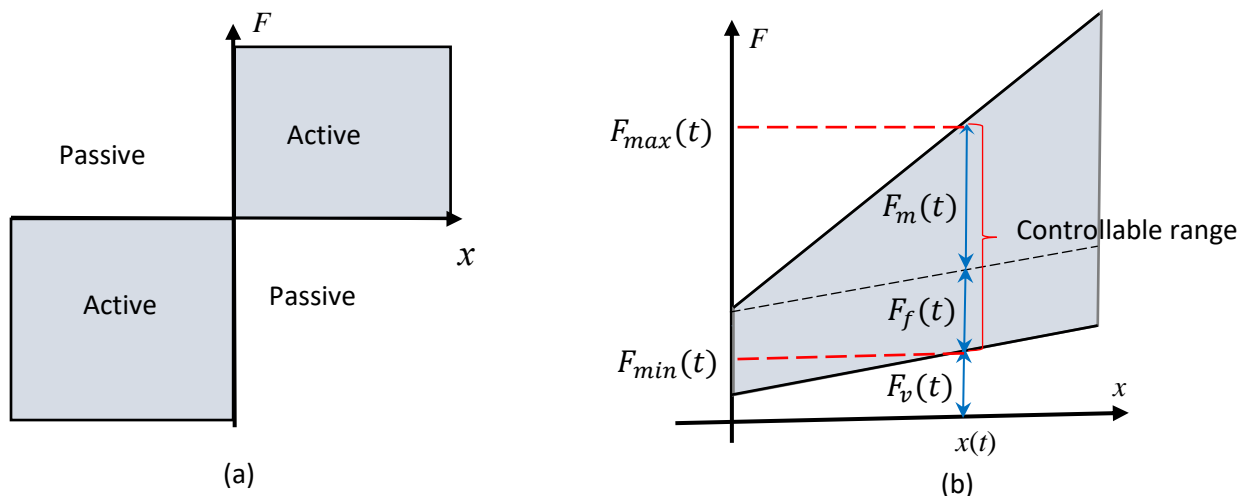

Figure 6.1 MRE-based isolator limitations: (a) on the semi-active control force generation, and (b) on minimum–maximum control force values.

$$F(t) = \begin{cases} F_{Desired}(t); & F_{Desired}(t)\,x(t) > 0 \\ F_{Passive}(t); & F_{Desired}(t)\,x(t) \leq 0 \end{cases} \tag{6.1}$$

In Eq. (6.1), $F_{Desired}(t)$ is the desired force determined by a semi-active algorithm, $F_{Passive}(t)$ is the passive force that occurs in the isolator without an electric current, and $x(t)$ is the displacement of the isolator.

Furthermore, the force that the MRE-base isolator can generate is bounded by the upper and lower limit values as follows.

$$|F_{min}(t)| \leq |F_{Desired}(t)| \leq |F_{max}(t)|, \tag{6.2}$$

In Eq. (6.2), $|F_{max}(t)|$ and $|F_{min}(t)|$ are the magnitudes of the maximum and minimum isolator forces corresponding to the maximum and minimum applied currents, respectively.

The variation range of the force generated by the MRE-based isolator is described in Figure 6.1(b). If the control force $F_{Desired}(t)$ falls within the range, the inverse model is used to calculate the optimal desired input current.

6.2 Inverse dynamic model of the isolator

The inverse model is necessary to describe the relationship between the desired force and the corresponding applied current/voltage [33, 34]. In this study, the inverse dynamics model for the MRE-based isolator is designed. Firstly, the displacement $x(t)$ and velocity $\dot{x}(t)$ are measured at time t, and the applied current $I(t-1)$ is measured at $t-1$. Based on the dynamic model represented by Eq. (3.11), the magnetic field-dependent variable stiffness force $F_m(t)$ is estimated as follows,

$$F_m(t) \approx F_{Desired}(t) - F_v(t) - F_f(t-1), \tag{6.3}$$

where $F_{Desired}(t)$ is the desired force that satisfies the constraint in Eq. (6.1, 6.2) at time t, $F_v(t)$ is the nominal viscoelastic force of the MRE, which can be calculated from Eq. (3.4) at t. While the friction $F_f(t)$ is the nonlinear function and depend on the applied current $I(t)$. The friction $F_f(t)$ can be approximated by $F_f(t-1)$, (where $F_f(t-1)$ is the friction force calculated from Eq. (3.9) at $t-1$). The above approximation is only affected by the accuracy of the friction force. In fact, as the gradient of the continuously changing current is small enough within a short time interval, the approximation of $F_f(t)$ by $F_f(t-1)$ is thought to be sufficiently reasonable when $\Delta t \to 0$.
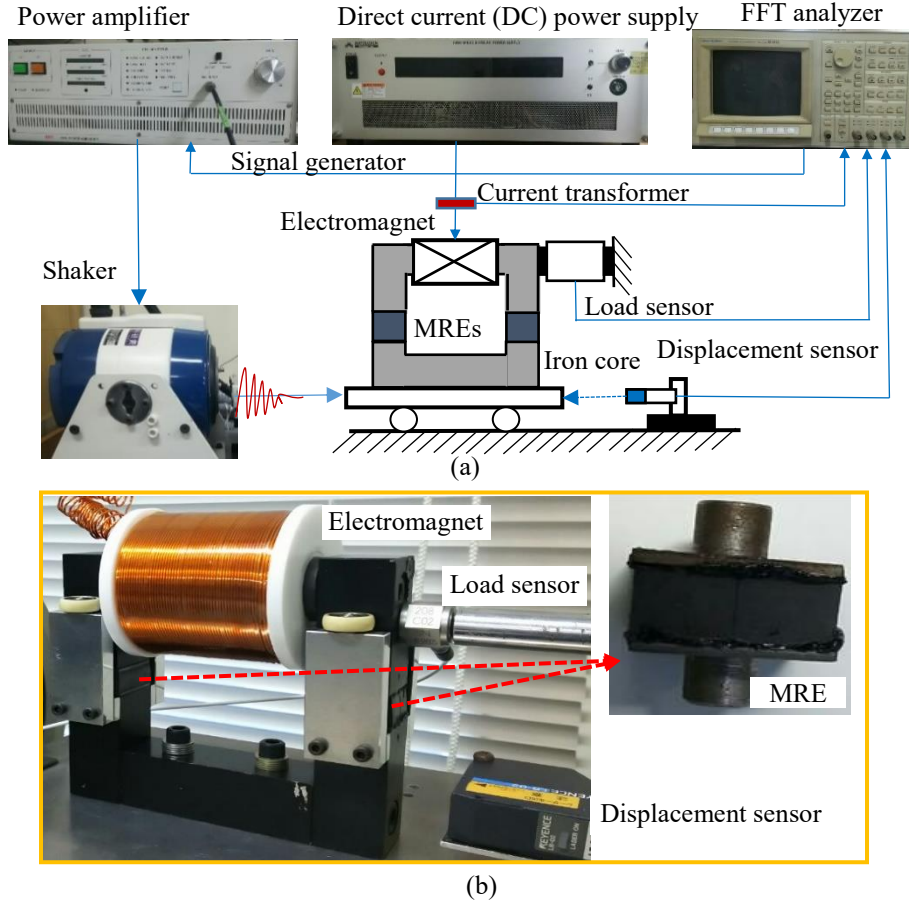
Figure 6.2 An experiment was conducted to evaluate the effectiveness of the inverse MRE model: (a) the experimental setup, and (b) photograph of the MRE-based isolator.

From Eq. (6.3) and Table 3.2, the applied current at time t is approximated by the following function,

$$-0.38I^2(t) + 4.25I(t) - \frac{F_m(t)}{x(t)} = 0, \tag{6.4}$$

where $F_m(t)$ is determined by Eq. (6.3), and $x(t)$ is measured by a displacement sensor.

The variable stiffness force $F_m(t)$ is a linear function with respect to displacement, and the ratio $F_m(t)/x(t)$ represents the variable stiffness K_m of the MRE. The singularity problem arises when the displacement approaches zero ($x(t) \approx 0$). Therefore, the ratio should be replaced by $\Delta F(t)/\Delta x(t)$ in which the numerator and the denominator values correspond to the differences in the force and displacement between the two time steps.

The experimental setup used to evaluate the effectiveness of the MRE inverse model is presented in Figure 6.2. The base was excited by a shaker whose excitation signal was supplied by a signal generator and a power amplifier. The isolator displacement was measured by a laser displacement sensor (KEYENCE LB-02), and the force response by a load sensor (PCB PIEZOTRONICS 208C02), respectively. The displacement, force, and applied current were recorded using a Fast Fourier Transform (FFT) spectrum

analyzer (ONOSOKI CF-6400). A direct current (DC) power supply (MATSUSADA PRECISION Inc., Series POP 65-5) was used to adjust the supply of DC current to a magnetic coil.

The inverse model was evaluated in two steps. Firstly, the experiment was performed under swept sine excitation within the frequency band of 5–30 Hz (Figure 6.3(a)). The applied current was adjusted randomly and manually within a range of 0–4 A (Figure 6.3(b)). The force response was measured as shown in Figure 6.3(c). In the second step, the displacement data and the force response data are used as inputs for the inverse model. The current variation predicted by the model was compared with the measured one. As shown in Figure 6.4, a good agreement is obtained between the predicted and measured currents. This result proves that the inverse model works effectively.
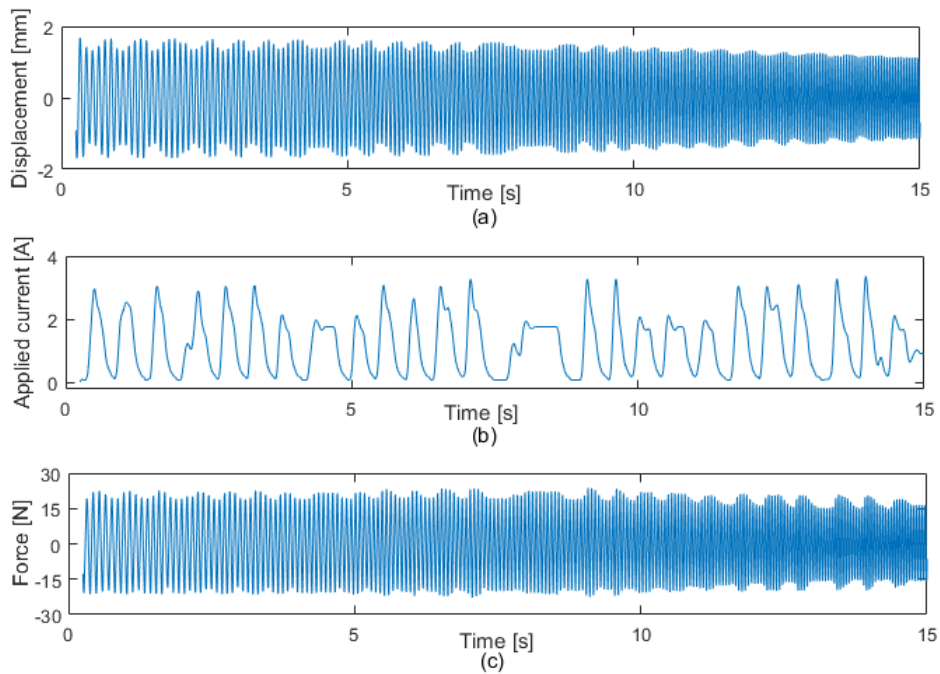

Figure 6.3. Measured time history data for the MRE inverse model: (a) displacement of the isolator, (b) electric current applied to the isolator, and (c) force generated by the isolator.
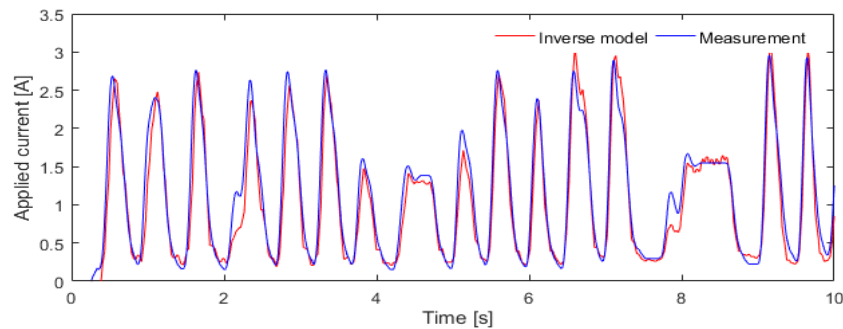

Figure 6.4 Comparison between the output of the inverse model and the manually adjusted electric current.
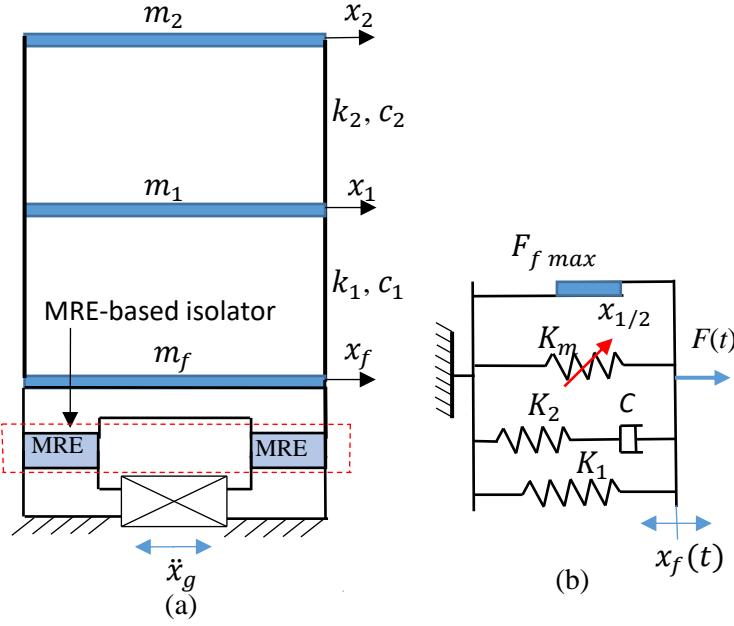
Figure 6.5 Schematic of the implemented MRE: (a) a two-story building structure, which employs an MRE-based isolator, and (b) the mechanical equivalent model of the MRE-based isolator.

6.3 Equation of motion

A two-story building model (m_1, m_2) with a fundament plate (m_f) rigidly connected to the MRE-based isolator as shown in Figure 6.5. Assuming the existence of an earthquake acceleration, $\ddot{x}_g$, the equation of motion can be written as follows:

$$M\ddot{x} + C\dot{x} + Kx = \Lambda F_{Desired} - M\Gamma\ddot{x}_g, \tag{6.5}$$

In Eq. (6.5), $x = \left[x_f, x_1, x_2\right]^T$ is a response vector, and x_1, x_2 denote the drifts of a designated ith story unit, and x_f is the displacement of the fundament plate (same as the isolator displacement), $F_{Desired}$ is the desired force generated by the isolator, $\Gamma = [1,1,1]^T$ is a vector that represents the influence of earthquake excitation, Λ is a 3×1 matrix that indicates the location of the control force, and M, C, and K, are 3×3 matrices with respect to mass, damping, and stiffness, defined as

$$M = \begin{bmatrix} m_f & 0 & 0 \\ 0 & m_1 & 0 \\ 0 & 0 & m_2 \end{bmatrix}, C = \begin{bmatrix} c_1 & -c_1 & 0 \\ -c_1 & c_1 + c_2 & -c_2 \\ 0 & -c_2 & c_2 \end{bmatrix}, K = \begin{bmatrix} k_1 & -k_1 & 0 \\ -k_1 & k_1 + k_2 & -k_2 \\ 0 & -k_2 & k_2 \end{bmatrix}.$$

6.4 Robust adaptive controller design

The objective of the controller design is to develop a control algorithm for the isolator having structural uncertainties in mass, damping, and stiffness, under the unknown earthquake excitation, such that the relative displacements are stabilized at zero.

The sliding surface S in the phase plane is defined as

$$S = \dot{x} + \lambda x = 0. \tag{6.6}$$

In Eq. (6.6), $\lambda > 0$ is the gain matrix to be determined such that the motion on the sliding surface becomes stable. The system dynamics regarding Eq. (6.5) can be written in terms of S as follows:

$$\dot{S} = M^{-1}\Lambda F_{Desired} - M^{-1}C\dot{x} - M^{-1}Kx + \lambda\dot{x} - \Gamma\ddot{x}_g. \tag{6.7}$$

We define $\psi = [\psi_1\ \psi_2\ \psi_3]^T = M^{-1}\Lambda$, and $P\xi = M^{-1}C\dot{x} + M^{-1}Kx$. The system dynamics can be rewritten as follows:

$$\dot{S} = \psi F_{Desired} - P\xi + \lambda\dot{x} - \Gamma\ddot{x}_g, \tag{6.8}$$

where $\xi = \left[k_1/m_f, k_1/m_1, k_2/m_1, k_2/m_2, c_1/m_f, c_1/m_1, c_2/m_1, c_2/m_2\right]^T$ is the parameter vector, and $P \in R^{3\times8}$ is the corresponding repressor vector, which is written explicitly as $P = [x_f - x_1, 0, 0, 0, \dot{x}_f - \dot{x}_1, 0, 0, 0; 0, -x_f + x_1, x_1 - x_2, 0, 0, -\dot{x}_f + \dot{x}_1, \dot{x}_1 - \dot{x}_2, 0; 0, 0, 0, x_1 - x_2, 0, 0, 0, \dot{x}_1 - \dot{x}_2]$.

Next, we define $\hat{\psi}$ and $\hat{\xi}$ as the estimated parameters. The force generated by the standard adaptive controller [35] can be determined according to the following equation:

$$F_{Desired} = -(\hat{\psi}^{-1})^T[kS - P\hat{\xi} + \lambda\dot{x}], \tag{6.9}$$

where $\hat{\psi}^{-1} = [1/\hat{\psi}_1, 1/\hat{\psi}_1, 1/\hat{\psi}_1]^T$, and k is the gain constant.

If the estimated parameter $\hat{\psi}$ in Eq. (6.9) reaches zero, the calculated control input $F_{Desired}$ may become very large. This disadvantage can be improved by using a novel robust adaptive controller. Therefore, when the estimated parameter approaches zero, the standard adaptive controller is temporarily replaced by the adaptive sliding controller F_s. The smooth switching algorithm is used to determine the control authority between the two controllers.

The smooth switching algorithm [36] is employed to observe the singularity,

$$\varphi_i = 1 - exp\left(-(\hat{\psi}_i/\delta)\right), \tag{6.10}$$

where δ is the width of the corresponding transition. The switching algorithm has the following characteristics for each vector component, given $i = 1, 2, 3$.

Chapter 6: Robust adaptive controller for semi-active control of uncertain structures using an MRE-based isolator

$$0 \leq \varphi_i \leq 1 \quad \forall \hat{\psi}_i \in R, \tag{6.11}$$

$$\lim_{\hat{\psi}_i \to 0} \varphi_i / \hat{\psi}_i = 0, \tag{6.12}$$

$$\lim_{|\hat{\psi}_i| \to \infty} \varphi_i / \hat{\psi}_i = 1. \tag{6.13}$$

Constitution of the robust adaptive controller seems to be appropriate if we consider the following three components: the standard adaptive linearizing controller F_a as a master controller, the adaptive sliding mode controller F_s used as a temporary controller during the singularity [37], and the single robust controller F_r used for the external disturbance. Therefore, $F_{Desired}$ is expressed as follows:

$$F_{Desired} = F_a + F_s + F_r, \tag{6.14}$$

where

$$F_a = -(\hat{\psi}^{-1})^T * I_\varphi * \left[kS - P\hat{\xi} + \lambda\dot{x}\right], \tag{6.15}$$

$$F_s = -\frac{1}{\Omega} * \text{sgn}(S^T) * \left(I_3 - I_\varphi\right) * \left|kS - P\hat{\xi} + \lambda\dot{x}\right|, \text{ and} \tag{6.16}$$

$$F_r = -\frac{1}{\Omega} * \text{sgn}(S^T) * \Gamma\left|\ddot{x}_g\right|, \tag{6.17}$$

and $\hat{\psi}$ and $\hat{\xi}$ represent the estimated values of ψ and ξ, respectively, $\tilde{\psi} = \hat{\psi} - \psi$ and $\tilde{\xi} = \hat{\xi} - \xi$ denote the estimation errors, and

$$I_\varphi = \begin{bmatrix} \varphi_1 & 0 & 0 \\ 0 & \varphi_2 & 0 \\ 0 & 0 & \varphi_3 \end{bmatrix}, \quad I_3 = \begin{bmatrix} 1 & 0 & 0 \\ 0 & 1 & 0 \\ 0 & 0 & 1 \end{bmatrix}.$$

Remark 1: The parameter Ω is positive definite and affects the efficiencies of the adaptive sliding mode and single robust controllers. Assume that Ω is known in advance and that satisfies $\Omega \leq \|\psi_{min}\|_2$, where $\|...\|_2$ is the 2-norm function and ψ_{min} is the lower bound for the parameter ψ.

Eq. (6.12) shows that the singularity problem will be avoided when $\hat{\psi}_i$ approaches zero, while Eq. (6.11) and Eq. (6.13) guarantee that the control inputs are bounded all the time. The following updated laws can then be given as follows:

$$\dot{\hat{\psi}} = \frac{1}{\alpha_1} S(\hat{\psi}^{-1})^T I_\varphi\left(kS - P\hat{\xi} + \lambda\dot{x}\right), \text{ and} \tag{6.18a}$$

$$\dot{\hat{\xi}} = -\frac{1}{\alpha_2} P^T S, \tag{6.18b}$$

where α_1 and α_2 are the tuning gains.

The proposed closed-loop controller is described in Figure 6.6. The components of the state vector $[x, \dot{x}]$, represent the displacement and velocity responses. The control scheme consists of three parts: a standard adaptive nonlinear controller F_a, an adaptive sliding mode controller F_s, and a single robust controller F_r. By using the switching algorithm between the standard adaptive controller and the adaptive sliding mode controller, the proposed controller gains better stability with lesser control force compared to the case where single controllers were used independently. The control force is limited within the controllable range of the isolator. The inverse model is then employed to obtain the applied current. Finally, the MRE-based isolator exerts an actual force on the two-story building.

Theorem: Consider the closed-loop system, including the dynamic motion represented by Eq. (6.8), the control algorithm represented by Eq. (6.14), and the adaptive algorithm represented by Eq. (6.18). Assume that the desired force, $F_{Desired}$, satisfies the limitations explained in Section 6.1. If the value of Ω is known in advance, and also if the gain k, α_1, and α_2, are all positive constants, then

T1) All the system values must be bounded for $\forall t \geq 0$ and

T2) The displacement $x(t) \to 0$ as $t \to \infty$.

Proof:

Choose the following Lyapunov function:

$$V(t) = \frac{1}{2}\left(S^T S + \alpha_1 \tilde{\psi}^T \tilde{\psi} + \alpha_2 \tilde{\xi}^T \tilde{\xi}\right) \tag{6.19}$$

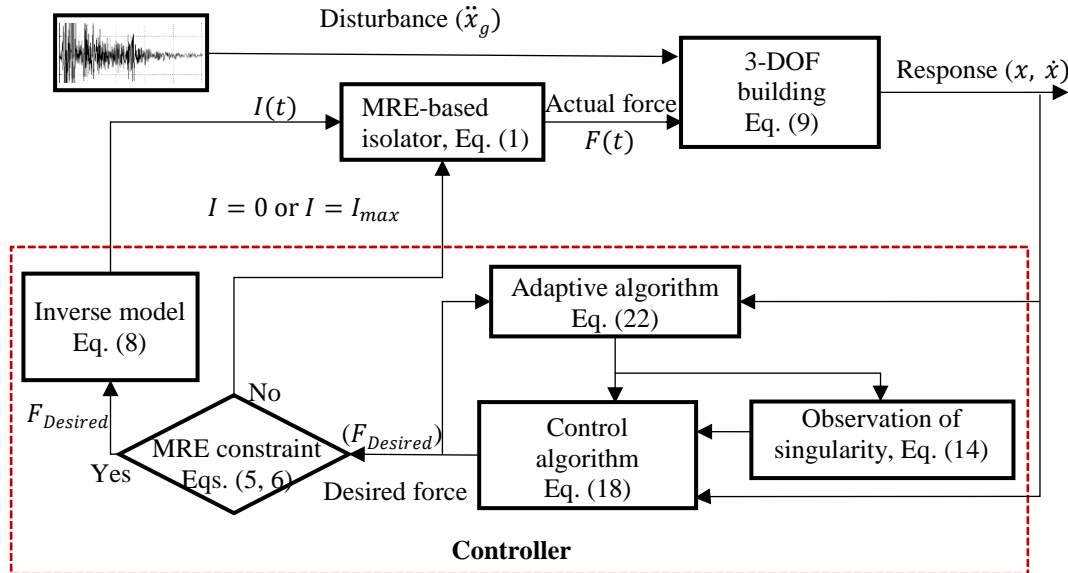Differentiation of Eq. (6.19) with respect to time, and use of Eq. (6.8) leads to

Figure 6.6. Diagram of closed-loop control system.

$$\dot{V}(t) = S^T \dot{S} + \alpha_1 \tilde{\psi}^T \dot{\tilde{\psi}} + \alpha_2 \tilde{\xi}^T \dot{\tilde{\xi}}$$

$$= S^T \left(\psi F_{Desired} - P\xi + \lambda \dot{x} - \Gamma \ddot{x}_g \right) + \alpha_1 \tilde{\psi}^T \dot{\tilde{\psi}} + \alpha_2 \tilde{\xi}^T \dot{\tilde{\xi}}$$

$$= S^T \left(\psi (F_a + F_s + F_r) - P(\hat{\xi} - \tilde{\xi}) + \lambda \dot{x} - \Gamma \ddot{x}_g \right) + \alpha_1 \tilde{\psi}^T \dot{\tilde{\psi}} + \alpha_2 \tilde{\xi}^T \dot{\tilde{\xi}}$$

$$= S^T \left(\psi (F_a + F_s + F_r) - P\hat{\xi} + \lambda \dot{x} - \Gamma \ddot{x}_g \right) - S^T \Gamma \ddot{x}_g + S^T P \tilde{\xi} + \alpha_1 \tilde{\psi}^T \dot{\tilde{\psi}} + \alpha_2 \tilde{\xi}^T \dot{\tilde{\xi}} \quad (6.20)$$

Equation (6.20) can be rewritten as

$$\dot{V}(t) = -kS^T S + S^T \psi (F_a + F_s + F_r) + S^T I_\varphi \left(kS - P\hat{\xi} + \lambda \dot{x} \right) + S^T (I_3 - I_\varphi) \left(kS - P\hat{\xi} + \lambda \dot{x} \right)$$

$$- S^T \Gamma \ddot{x}_g + S^T P \tilde{\xi} + \alpha_1 \tilde{\psi}^T \dot{\tilde{\psi}} + \alpha_2 \tilde{\xi}^T \dot{\tilde{\xi}}. \quad (6.21)$$

Taking Eqs. (6.15)–(6.18) into account, and noting that $\Omega \le \|\psi_{min}\|_2$, we have

$$S^T \psi F_a = S^T \left[(\hat{\psi} - \tilde{\psi}) F_a \right]$$

$$= -S^T \hat{\psi} (\hat{\psi}^{-1})^T I_\varphi \left(kS - P\hat{\xi} + \lambda \dot{x} \right) + S^T \tilde{\psi} (\hat{\psi}^{-1})^T I_\varphi (kS - P\hat{\xi} + \lambda \dot{x})$$

$$= -S^T I_\varphi \left(kS - P\hat{\xi} + \lambda \dot{x} \right) + \tilde{\psi}^T \left[S (\hat{\psi}^{-1})^T I_\varphi \left(kS - P\hat{\xi} + \lambda \dot{x} \right) \right]$$

$$= -S^T I_\varphi \left(kS - P\hat{\xi} + \lambda \dot{x} \right) - \alpha_1 \tilde{\psi}^T \dot{\hat{\psi}}, \quad (6.22)$$

$$S^T \psi F_s = S^T \psi * \left[-\frac{1}{\Omega} \operatorname{sgn}(S^T) \left(I_3 - I_\varphi \right) \left| kS - P\hat{\xi} + \lambda \dot{x} \right| \right]$$

$$= -\frac{1}{\Omega} \psi^T S \operatorname{sgn}(S^T) \left(I_3 - I_\varphi \right) \left| kS - P\hat{\xi} + \lambda \dot{x} \right|$$

$$\le -|S^T| \left(I_3 - I_\varphi \right) \left| kS - P\hat{\xi} + \lambda \dot{x} \right|$$

$$\le -S^T (I_3 - I_\varphi) \left(kS - P\hat{\xi} + \lambda \dot{x} \right), \quad (6.23)$$

$$S^T \psi F_r = S^T \psi * \left[-\frac{1}{\Omega} \operatorname{sgn}(S^T) \Gamma |\ddot{x}_g| \right],$$

$$= -\frac{1}{\Omega} \psi^T S \operatorname{sgn}(S^T) \Gamma |\ddot{x}_g|$$

$$\le -|S^T| \Gamma |\ddot{x}_g|$$

$$\le -S^T \Gamma \ddot{x}_g, \text{ and} \quad (6.24)$$

$$S^T P \tilde{\xi} + \alpha_2 \tilde{\xi}^T \dot{\tilde{\xi}} = \tilde{\xi}^T \left(P^T S + \alpha_2 \dot{\tilde{\xi}} \right) = 0 \quad (6.25)$$

For clarifying Eqs. (6.23) and (6.24), we have

$$\psi^T S \operatorname{sgn}(S^T) = \psi^T [1 \ 1 \ 1]^T |S|^T$$

$$= (\psi_1 + \psi_2 + \psi_3) |S|^T \ge \sqrt{\psi_1^2 + \psi_2^2 + \psi_1^2} \, |S|^T \ge \Omega \, |S|^T . \quad (6.26)$$

Therefore, by substituting Eqs. (6.22)–(6.25) into Eq. (6.21), we obtain the following equation:

$$\dot{V}(t) \le -kS^T S \quad (6.27)$$

The Lyapunov function $V(t)$ is a nonincreasing function. As the values of $S, \tilde{\psi}$, and $\tilde{\xi}$ are bounded, the estimated values of $\hat{\psi}$ and $\hat{\xi}$ are also bounded by definition. By integrating Eq. (6.27) from 0 to t, we have

$$\int_0^t \dot{V}(\tau)d\tau = V(t) - V(0) \leq -\int_0^t kS(\tau)^T S(\tau)d\tau \tag{6.28}$$

Because $V(0)$ is bounded and $V(t)$ is nonincreasing and also bounded,

$$\lim_{t \to \infty} \int_0^t kS(\tau)^T S(\tau)d\tau < \infty. \tag{6.29}$$

According to Barbalat's lemma, we can show that $\lim_{t \to \infty} kS(\tau)^T S(\tau)d\tau = 0$, and that $\lim_{t \to \infty} S(t) = 0$ and $\lim_{t \to \infty} x(t) = 0$. This implies that the displacement $x(t)$ will converge to zero asymptotically.

**6.5 Numerical evaluation of the control performance**

In this section, simulations are discussed to demonstrate the effectiveness of the proposed controller. The parameter values assigned to the variables of the numerical model are $m_f = 3$ kg, $m_1 = 3$ kg, $m_2 = 3$ kg, $k_1 = k_2 = 10^4 \, N \, m^{-1}$, $c_1 = c_2 = 2 \, N \, s \, m^{-1}$, $\lambda = 2I$, $\alpha_1 = 1, \alpha_2 = 2$, $k = 1$, $\delta = 0.1$, $\Lambda = [1, 0, 0]^T$ and $\Omega = 0.1$. The structure is exposed under El Centro earthquake.

The elicited results of the second floor displacement and the control forces generated by the respective controllers are depicted in Figures 6.7 and 6.8. Figure 6.7 shows that the displacement can be reduced with the use of single-type controllers. However, the single controllers have some drawbacks, including the fact that the standard adaptive controller causes large displacements in the early stages of control, and also that the sliding mode controller produces significant chattering, as shown in Figure 6.7(a). These problems can be noticeably reduced by using the proposed controller, as shown in Figure 6.7(b). As explained in Section 6.4, the proposed algorithm is expected to reduce the control force compared to the standard adaptive algorithm.
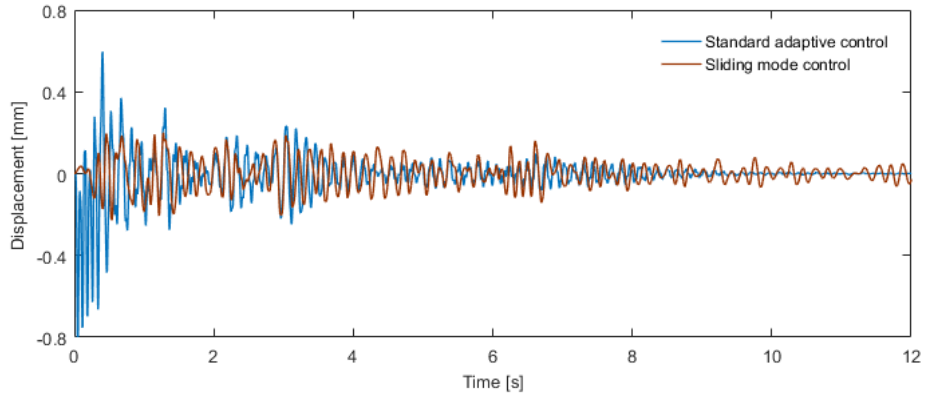
(a)
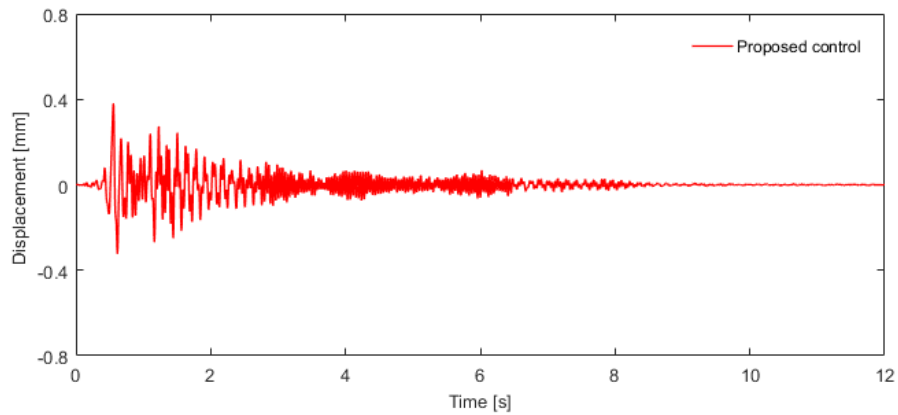
(b)

Figure 6.7 The displacement responses under El Centro earthquake: (a) with standard adaptive control and adaptive sliding mode control and (b) with the proposed control.
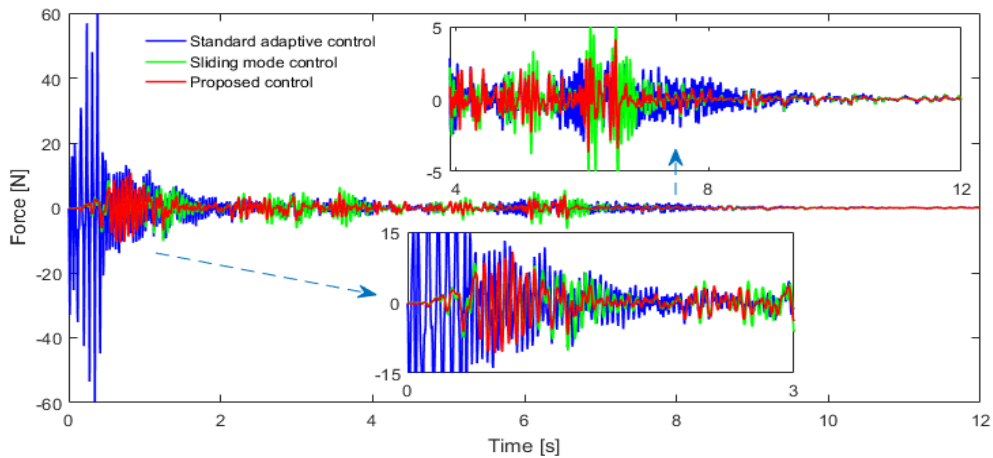

Figure 6.8 Comparison of the desired control forces elicited when different algorithms are used.

Figure 6.9 Time history of the parameter error $\tilde{\psi}$.
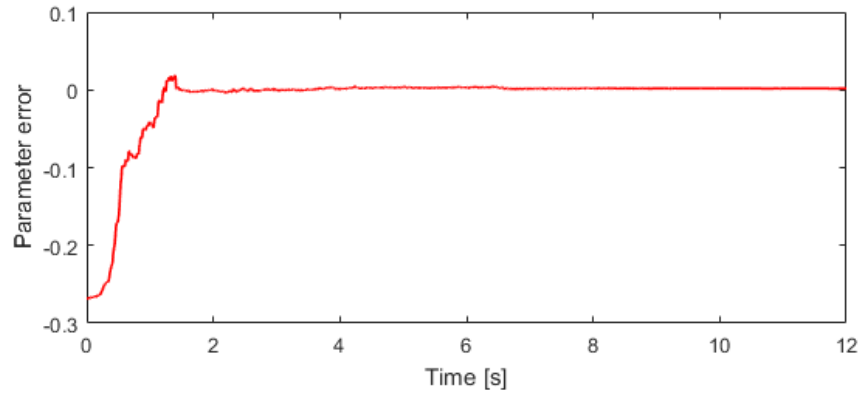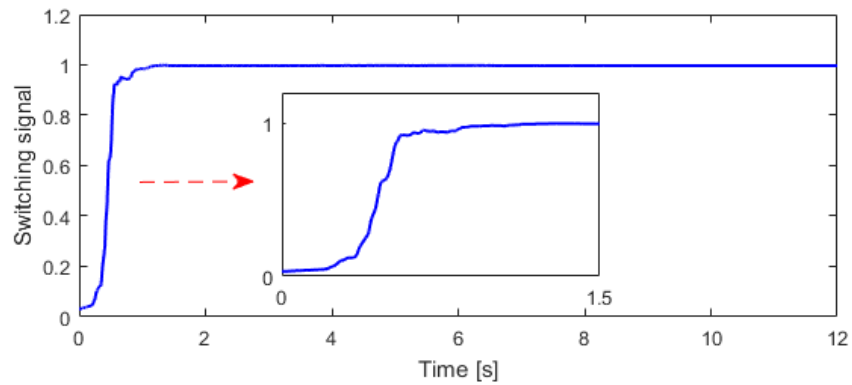

Figure 6.10 Time history of the switching signal. In the case of large parameter errors (small switching signal), the control force F_s dominates, whereas the force F_a takes over when the error approaches zero.
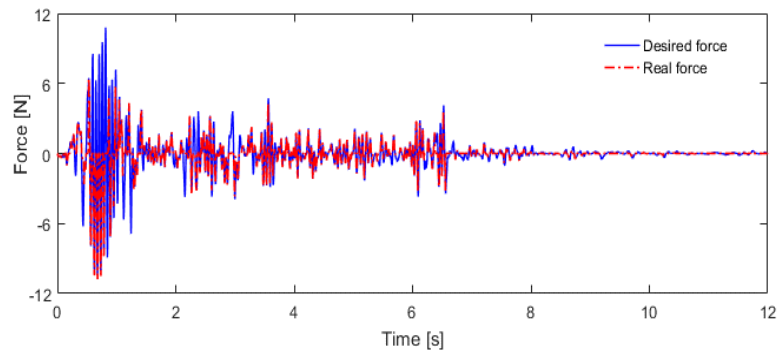

Figure 6.11 Comparison between the desired and actual forces. The real force is the desired force component that satisfies the isolator limitations.
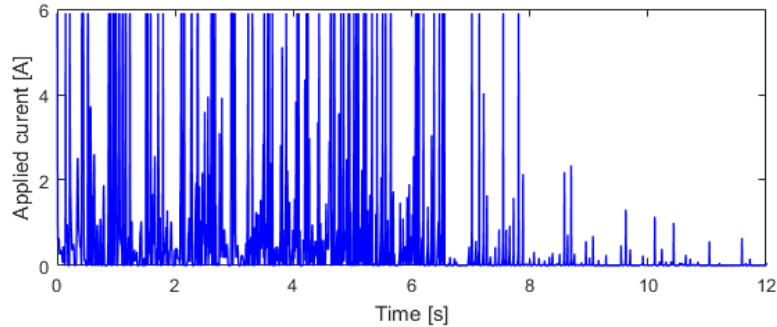
Figure 6.12 Applied electric current in the MRE-based isolator based on the use of the inverse model.

The control forces calculated by three different control algorithms are compared in Figure 6.8. The adaptive controller requires that the control force is as high as the maximal value of 60 N. In contrast, the maximal control force is less than 10 N when the proposed controller is used.

The parameter error and switching signal are shown in Figure 6.9 and 6.10, respectively. The parameter error converges to zero after 1 s, and the value of the corresponding switching signal is changed from 0 to 1. Figure 6.11 describes the actual force generated by the MRE-based isolator. It is the desired force component that satisfies the limitation based on which the generated force in the isolator is restricted. The satisfaction level is found to be 75%. Figure 6.12 shows the applied current that is determined from the actual force and the isolator motion in accordance to the use of the inverse model. These results demonstrate that the proposed controller has advantages compared to the single controllers in terms of the improved displacement reduction performance with fewer control force requirements.

The effectiveness of the proposed controller can be explained based on its working mechanism. In the early stage of control, since the adaptive sliding controller works dominantly to mitigate vibration, the control force is determined based on the bounded parameters. In this period, the standard adaptive controller works as a virtual controller, and the dynamic parameters are updated continuously. When the parameters approach zero, the standard adaptive controller gains an advantage compared to the proposed controller in controlling the system. The smooth switching algorithm is used to monitor the estimated parameters and decides the priority. In this way, the advantages of the single controllers are exploited and their drawbacks are eliminated. The proposed controller is effective in reducing vibration with lesser effort for control force generation. Therefore, the controller is suitable for the MRE-based isolator in the reduction of seismic responses.

The performances of the passive controller, fuzzy controller, and the proposed controller, are compared in terms of the scaled El Centro earthquake excitation. The responses of the two-story building are shown in Figure 6.13 and 6.14. The relative displacement response is significantly reduced when using two semi-active controllers. The proposed controller works remarkably better than the fuzzy controller. Furthermore,

the second floor acceleration response is suppressed in the system with semi-active controllers, as shown in Figure 6.13(b). The proposed controller works moderately better than the fuzzy controller. The peak of the relative displacement and the acceleration are shown in Figure 6.14. Better performances can be elicited from the isolated building using the proposed controller.
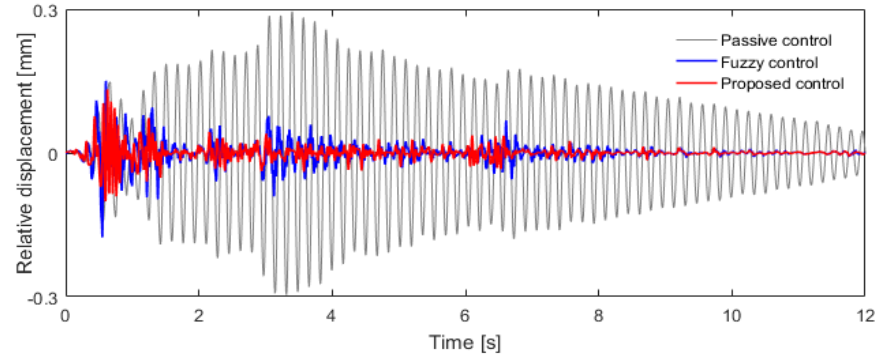
(a)
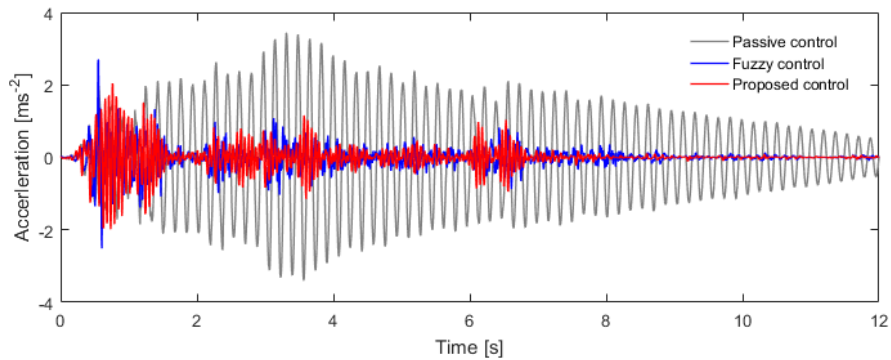
(b)

Figure 6.13 The relative displacement and acceleration responses of the second floor following the El Centro earthquake: (a) relative displacement response, and (b) acceleration response.
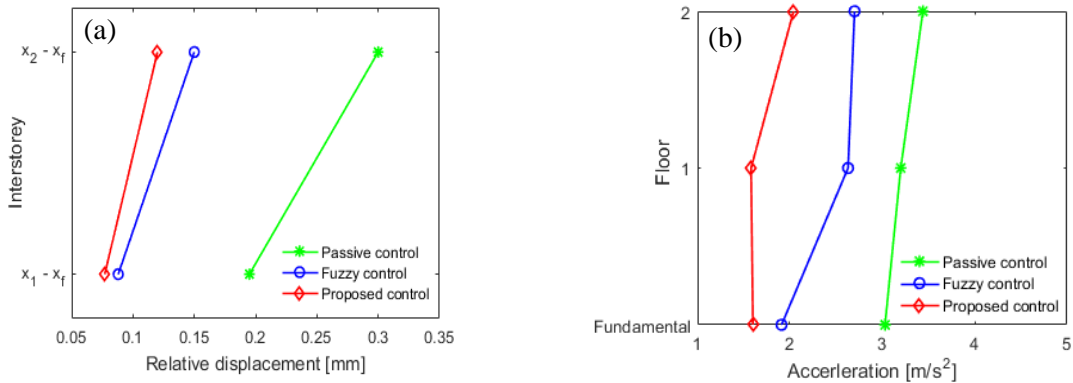
Figure 6.14 The maximum relative displacements and accelerations of the two-story building: (a) relative displacements, and (b) accelerations.

6.6 Summary

A robust adaptive controller was then proposed for the semi-active isolator to reduce seismic vibration. The robust adaptive controller suppressed significantly structural responses with uncertain parameters. Furthermore, the proposed controller requires lesser control force than the standard adaptive controller. The proposed controller overcomes the drawbacks of the conventional semi-active controller, avoids the singularity problem, and provides robust stability.

Chapter 7

Summary, Conclusion and Recommendations.

7.1 Summary of the work

This research was aimed at investigating a MRE-based isolator in the field of modeling and vibration control by a proposed dynamic model and innovative semi-active controllers. The major achievements of this study are summarized as follows:

- The dynamic viscoelastic characteristic of MRE-based isolator was presented. The MRE properties are strongly nonlinear functions of magnetic flux density, displacement amplitude, and the excitation frequency.

- The dynamic viscoelastic model of the MRE-based isolator was presented, and a procedure to determine the six model parameters was introduced. The force-displacement relationship obtained by the numerical model is nearly consistent with the measurement results. Moreover, the proposed model predicts with high accuracy the dynamic viscoelastic characteristics of MRE in a wide range of frequencies (3–30 Hz) and shear strain (4%–16%).

- A fuzzy control algorithm was used to enhance performance of the MRE-based isolator in a structure under seismic excitation. Both numerical simulation and experimental results show that the "fuzzy semi-active control" provides better performance than the rest of the passive cases, "fixed base," "passive off," and "passive on." The peaks of the third mass displacement and absolute acceleration are reduced by 15% and 24%, respectively. The maximum relative displacement between third mass and fundament plate also decreases by 30%. The MRE-based isolator used in conjunction with the fuzzy controller is efficient for mitigating vibrations in a two story building.

- The results showed that the fuzzy semi-active controller overcame the drawback of traditional semi-active control in reducing chattering.

- The inverse model of an MRE-based isolator was derived. A good agreement is obtained between the predicted and measured electric currents to be supplied to a magnetic coil. This result proves that the inverse model works effectively.

- A robust adaptive controller was proposed for the semi-active isolator to reduce seismic vibration. The controller suppressed significantly structural responses with uncertain parameters. Furthermore, the proposed controller requires lesser control force than the standard adaptive

controller. The proposed controller overcomes the drawbacks of the conventional semi-active controller, avoids the singularity problem, and provides robust stability.

7.2 Conclusion

A series of studies reported in this thesis are intended to provide a deeper insight into the behavior of magnetorheological elastomer and their potential application in vibration control. In addition, new methods about modelling and control of dynamic systems by using MRE were proposed. The outcomes of this study are expected to provide useful information for developing MRE-based semi-active isolator in vibration control of a real structure. The main findings from this study can be summarized as follows:

- Magnetorheological elastomer (MRE) is a smart materials that mainly generate a slightly magnetic field dependent variable stiffness. MRE properties are strongly nonlinear functions of magnetic flux density and displacement amplitude, and slightly the function of frequency.

- The MRE-based isolators can be used effectively to govern the transmissibility of the structure by adjusting their properties. The results shown that the transmissibility of the scaled building is reduced significantly and the first natural frequency shifts from 7.6 Hz to 10.1 Hz by switching applied current.

- The proposed model captured accurately the dynamic viscoelastic characteristics of MRE for any desired combination of applied current, amplitude, and frequency. The numerical model is useful to design MRE-based isolator systems for various technical applications.

- A semi-active fuzzy controller can be used to enhance performance of the MRE-based isolator. The controller overcame the fast switching of the on-off algorithm that causes high acceleration and jerk peaks periodically.

- An inverse model is necessary for control system so that the structure is controlled by a desired control force. By using the inverse model, the advanced control algorithms can be developed for semi-active controllers.

- A robust adaptive controller for semi-active control is expected for a nonlinear system with unknown dynamic parameters. The results have shown that the controller overcame the drawbacks of the conventional semi-active controller, avoided the singularity problem, and provided robust stability.

- The simulation results have shown that the robust adaptive controller worked remarkably better than the fuzzy controller in protecting a two-story shear building during seismic events.

7.3 Recommendations for Future Work

The research performed in this study has significantly contributed to the implementation of MRE-based isolator in semi-active vibration systems. However, limitations of the present work are identified. The mechanical properties of MRE is limited; the natural frequency of the system is variable only in a narrow frequency band. The accuracy of the model in chapter 3 reduces in low frequency and low amplitude level. The inverse model in chapter 6 does not have enough accuracy in predicting electric current. The effectiveness of the robust adaptive controller has just been evaluated in simulation. Hence, the following suggestions are made for further developing the work which has been done in this thesis:

- Extend the mechanical properties of MRE by optimal the fabrication process and optimal the magnetic system.

- Improve the MRE model so that the model can work effectively in low frequency and low amplitude.

- Propose a new inverse model with high accuracy.

- Real-time control needs to be implemented to the robust adaptive controller for comprehensive evaluation.

References

[1] J.M. Ginder, M.E. Nichols, L.D. Elie, J.L. Tardiff, Magnetorheological elastomers: properties and applications, Proceedings of SPIE 3675, Smart Structures and Materials 1999: Smart Materials Technologies, Newport Beach, USA, July 1999, pp. 131–138.

[2] T. Komatsuzaki, Y. Iwata, Design of a real-time adaptively tuned dynamic vibration absorber with a variable stiffness property using magnetorheological elastomer. Shock and Vibration 2015, Article ID 676508.

[3] G.J. Liao, X.L. Gong, S.H. Xuan, C J. Kang, L.H. Zong, Development of a real-time tunable stiffness and damping vibration isolator based on magnetorheological elastomer. Journal of Intelligent Material Systems and Structures 23(1) (2011) 25-33. doi: 10.1177/1045389X11429853.

[4] M.R. Jolly, J.D. Carlson, B.C. Munoz and Bullions T A 1996 The magnetoviscoelastic response of elastomer composites consisting of ferrous particles embedded in a polymer matrix J. Intell. Mater. Syst. Struct. 7 613-22

[5] L. Chen, X.L. Gong, W.H. Li, Microstructures and viscoelastic properties of anisotropic magnetorheological elastomers, Smart Mater. Struct. 16 (2007) 1–6

[6] X.L. Gong, X.Z. Zhang, and P. Q. Zhang, "Fabrication and characterization of isotropic magnetorheological elastomers," *Polymer Testing*, vol. 24, no. 5, pp. 669–676, 2005.

[7] X. Zhang, S. Peng, W.Wen, and W. Li, "Analysis and fabrication of patterned magnetorheological elastomers," *Smart Materials and Structures*, vol. 17, no. 4, Article ID045001, pp. 1–5, 2008.

[8] M. Behrooz, X. Wang, F. Gordaninejad, Modeling of a new semi-active/passive magnetorheological elastomer isolator, Smart Material and Structures, Smart Mater. Struct. 23 (2014) 045013 (7pp).

[9] T. Komatsuzaki, T. Inoue, O. Terashima, Broadband vibration control of a structure by using a magnetorheological elastomer-based tuned dynamic absorber, Mechatronics 000(2016) 1-9.

[10] Y. Li, J. Li, T. Tian, W. Li, A highly adjustable magnetorheological elastomer base isolator for applications of real-time adaptive control, Smart Mater. Struct. 22 (2013) 095020 (18pp).

[11] M. Lokander, B. Stenberg. Improving the magnetorheological effect in isotropic magnetorheological rubber materials. Polym Test 2003; 22:677–80.

[12] T. Shiga, A. Okada, T. Kurauchi. Magnetroviscoelastic behavior of composite gels. J Appl Polym Sci 2003;B(4):787–92 .

[13] G.Y. Zhou. Shear Properties of a magnetorheological elastomer. Smart Mater Struct 2003; 12:139–46.

[14] A.V. Chertovich, G.V. Stepanov , Kramarenko EY , Khokhlov AR . New composite elastomers with giant magnetic response. Macromol Mater Eng 2010:336–41.

[15] G. Liao, X. Gong, S. Xuan, C. Kang, & L. Zong. 2012, 'Development of a real-time tunable stiffness and damping vibration isolator based on magnetorheological elastomer', Journal of Intelligent Material Systems and Structures, vol. 23, no. 1, pp. 25-33.

[16] H.-J.Jung, S.-H. Eem, D.-D. Jang, & J.-H. Koo, 2011, 'Seismic performance analysis of a smart base-isolation system considering dynamics of MR elastomers', Journal of Intelligent Material Systems and Structures, vol. 22, no. 13, pp. 1439-50.

[17] M. Behrooz, X. Wang, & F. Gordaninejad, 2014b, 'Performance of a new magnetorheological elastomer isolation system', Smart Materials and Structures, vol. 23, no. 4, p. 045014.

[18] J. Yang, S. Sun, T. Tian, W. Li, H. Du, G. Alici, M. Nakano, Development of a novel multi-layer MRE isolator for suppression of building vibrations under seismic, Mechanical Systems and Signal Processing, 70-71 (2016), pp. 811-820.

[19] X. B. Nguyen, T. Komatsuzaki, Y. Iwata, H. Asanuma, Fuzzy Semiactive Vibration Control of Structures Using Magnetorheological Elastomer, Shock and Vibration, Vol. 2017, Article ID 3651057, 15 pages.

[22] R. Li, L. Z. Sun, Dynamic viscoelastic modeling of magnetorheological elastomers, Acta Mech, 225 (2014), pp. 1347-1359.

[22] W. H. Li, Y. Zhou, T. F. Tian, Viscoelastic of MR elastomers under harmonic loading, Rheol Acta, 49 (2010), pp. 733-740.

[23] S. H. Eem, H. J. Jung, Jung, J. H. Jung, Modeling of magneto-rheological elastomers for harmonic shear deformation, IEEE transactions on magnetics, 48 (11) (2012), pp. 3080-3083.

[24] J. Yang, H. Du, W. Li, Y. Li, J. Li, S. Sun, H. X. Deng, Experimental study and modeling of a novel magnetorheological elastomer isolator, Smart Materials and Structures, 22 (11) (2013), pp. 1-14.

[25] M. Norouzi, S. M. S. Alehashem, H. Vatandoost, M. M. Shahmardan, A new approach for modeling of magnetorheological elastomers, Journal of Intelligent Material Systems and Structures, 27(8) (2016), pp. 1121-1135.

[26] G.J. Liao, X.L. Gong, C.J. Kang, S.H. Xuan, The design of an active-adaptive tuned vibration absorber based on magnetorheological elastomer and its vibration attenuation performance, Smart Mater. Struct. 20 (07) (2011) 5015–5025.

[27] W. Zhu, X.-T. Rui, Semiactive Vibration Control Using a Magnetorheological damper and a magnetorheological elastomer based on the Bouc–Wen nodel, Shock and Vib., vol. 2014, Article ID 405421.

[28] S. Opie, W. Yim, Design and control of a real-time variable modulus vibration isolator, J. Intell. Mater. Syst. Struct. 22 (2) (2010) 113–125.

[29] L.M. Jansen, S.J. Dyke, Semi-active control strategies for MR dampers: A comparative study. J. of Eng. Mech. ASCE 2000; 126(8):795–803.

[30] K.M. Choi, S.W. Cho, H.J. Jung, I.W. Lee, Semi-active fuzzy control for seismic response reduction using magnetorheological dampers, Earthq. Eng. Struct. Dyn. 33 (2004) 723–736.

[31] J. Yang, S. Sun, T. Tian, W. Li, H. Du, G. Alici, M. Nakano, Development of a novel multi-layer MRE isolator for suppression of building vibrations under seismic, Mech. Syst. Signal Process. 70–71 (2016) 811–820.

[32] W. Zhu, X.-T. Rui, Semiactive Vibration Control Using a Magnetorheological damper and a magnetorheological elastomer based on the Bouc–Wen nodel, Shock and Vib., vol. 2014, Article ID 405421.